ROADVIEW

Robust Automated Driving in Extreme Weather

Project No. 101069576

Deliverable 3.5

Library of internal sensor noise models and compound noise modelling methodology

WP3 – Validated sensor and sensor noise models for synthetic environments

Authors	Pak Hung Chan (WMG), Hamed Haghighi (WMG), Heikki Hyyti (FGI), Valentina Donzella (WMG)
Lead participant	WMG
Delivery date	24 February 2025
Dissemination level	Public
Type	Other

Version 1.0

Co-funded by the European Union

Innovate UK

Co-funded by the European Union. Views and opinions expressed are however those of the author(s) only and do not necessarily reflect those of the European Union or European Climate, Infrastructure and Environment Executive Agency (CINEA). Neither the European Union nor the granting authority can be held responsible for them. Project grant no. 101069576.

UK participants in this project are co-funded by Innovate UK under contract No.10045139.
Swiss participants in this project are co-funded by the Swiss State Secretariat for Education, Research and Innovation (SERI) under contract No. 22.00123.

Revision history

Author(s)	Description	Date
Pak Hung Chan (WMG), Hamed Haghighi (WMG), Heikki Hyyti (FGI), Valentina Donzella (WMG)	Draft deliverable v0.1	03/02/2025
Martin Sanfridson (RISE)	Review of v0.1	08/02/2025
Pak Hung Chan (WMG), Hamed Haghighi (WMG), Heikki Hyyti (FGI), Valentina Donzella (WMG)	Updated draft v0.2	13/02/2025
Amine Ben-Daoued (CE)	Review of v0.2	18/02/2025
Pak Hung Chan (WMG), Hamed Haghighi (WMG), Heikki Hyyti (FGI), Valentina Donzella (WMG)	V1.0 Complete	24/02/2025
Johannes Ripperger (accelCH)	Final checks and formatting	24/02/2025

Contents

List of Figures

List of Tables

Partner short names

LUA	Lapin Ammattikorkeakoulu OY
THI	Technische Hochschule Ingolstadt
CE	Centre d'études et d'expertise sur les risques, l'environnement, la mobilité et l'aménagement
RISE	RISE Research Institutes of Sweden AB
FGI	Maanmittauslaitos – Finnish Geospatial Research Institute
WMG	The University of Warwick
accelCH	accelopment Schweiz AG

Abbreviations

3-D	Three-Dimensional
AAD	Assisted and Automated Driving
BCP	Brown-Conrady Polynomial
CNF	Compound Noise Factor
D	Deliverable
FoV	Field of View
RCS	Radar Cross Section
SNR	Signal-to-Noise Ratio
T	Task
WP	Work Package
XiL	Anything-in-the-loop

Executive summary

Objectives

The objective of this deliverable is to describe the methodology to analyse and compound different noise factors affecting the performance of the different perception sensors considered in the ROADVIEW pipeline, i.e. LiDAR, 4D-RADAR, and camera. In the compounding process, the weather noise models (i.e. rain, fog, and snow) created by ROADVIEW Task 3.4 are combined with other sources of noise (e.g. obstructions, wind, luminosity, etc.), to create more realistic output sensors' data. Moreover, the deliverable also describes the procedure of measuring and creating LiDAR internal noise models, which are scarcely documented in Literature. A library of noise models is created as a part of this task, and this deliverable describes the selection of ROADVIEW noise models for compounding and demonstrates their application to data produced as apart of Task 3.7 and Task 3.2.

Similar to the models in Task 3.4, the compounded models generated by this task (i.e. Task 3.5) can be integrated into any simulation pipeline, and for ROADVIEW they are specifically used in WP7, supporting the virtual testing and more in general XiL testing. This deliverable created a library of 30 compounded noise models and shows their application to ROADVIEW sensor data.

Methodology and implementation

The deliverable describes a systematic approach to break down, analyse, model and compound different noise factors affecting the deployed automotive perception sensors technologies, namely camera, LiDAR, and 4D-RADAR. The approach allows for a thorough understanding of different noise sources and their potential interactions, similarities, and differences. Based on this approach, 10 additional noise models were selected, adapted, or created specifically for ROADVIEW, and then each one of them was combined with different weather noise models, created specifically for ROADVIEW in Task 3.4. For the above-mentioned additional noise models, the report describes how they have been created, selected, and curated for compounding. The specific methodology to compound noise models depends on the specific models that are combined and is described in this report. The methodology of compounding is demonstrated through application of the 30 compounded noise models onto ROADVIEW sensor data. Moreover, based on the specific noise models and their compounding, corner cases are identified where combining noise models causes significant data loss.

Outcomes

This task has produced: a framework to break down noise factors affecting the performance of perception sensors and to identify and determine the method to compound multiple noise models; a library of 30 curated noise models that can be applied to any real or simulated sensor data. As a part of this library, and specifically for LiDAR, the laser alignment error and power variability for LiDAR was systematically measured and parameterised to account for internal noise factors. The creation of compounded noise models enables to understand that they will impact the quality of the sensor data to a different degree and helps to identify corner cases in which the combination of noise factors has significant implications on the data. The compounded noise models will feed into WP7 and be considered in Task 7.6 to enhance the virtual testing environment.

Next steps

The developed framework and library will be carefully considered to support WP7 testing of the ROADVIEW system and be integrated into the simulation environment. Additionally, these models can be considered to augment and increase the value of existing datasets for such as the REHEARSE dataset, Suitable academic and industrial events will be explored for dissemination of the compounding methodology.

1 Introduction

The use of digital assets to support virtual testing (whether in fully simulated testing or with mixed reality testing) is an important component for the end-to-end development for ROADVIEW. In particular, having a virtual scene which can be used to generate realistic sensor data is particularly important, whether for development of algorithms or for XiL (anything-in-the-loop) testing of the full ROADVIEW pipeline in a controlled manner.

Previous tasks in ROADVIEW WP3 have tackled the creation of digital assets, such as testing facilities, testing targets, models of sensors including validated output data degradation due to rain, fog, and snow for automotive camera, LiDAR and 4D RADAR. From accurately generating digital assets of testing facilities where mixed reality and controlled real-world testing will take place (see D3.1), to the weather noise modelling using data-driven and physics-based methods (D3.3 and D3.4), to enable the testing and development of robust automated systems under harsh weather conditions [1] [2] [3]. However, in the real world, sensors are not subjected to one noise condition but multiple at the same time, i.e. there is not only rain or fog or snow affecting sensor performance, but a multitude of noise factors acting concurrently. Many works have focused on modelling one noise factor in isolation; however, the effect of multiple noise factors can potentially change the data drastically, resulting in a more significant impact on the next perception step, thus affecting the simulation-to-reality gap.

This deliverable describes the WMG compounding methodology to combine in simulation multiple noise factors affecting perception sensors performance. The methodology starts from the breakdown of different sources of noise on a specific sensor technology, namely for ROADVIEW we considered camera, LIDAR, and 4D RADAR. Then, for each identified noise factor, we consider how they can be combined. The combination of multiple sources of noise requires an understanding of how they affect the sensor output and how to 'order' or 'combine' them in the signal processing pipeline. For the considered automotive sensors, a series of 30 compounded noise models is presented, each one of them is a combination of a weather noise model from D3.4 and another different noise model, selected based on the carried-out noise factors' analysis. Specifically for LiDAR, a data driven approach was followed by FGI to model internal noise factors of alignment and power errors. For the other noise models, different techniques were selected: machine learning, data driven approaches, physics based, depending on the specific noise and available resources.

The report firstly represents the methodology for compounding with a breakdown of noise factors in chapter 2, and the framework to compound noise models in chapter 3, then discusses the modelling of internal LiDAR noise in chapter 4, presenting the results of the 30 compounded models in chapter 5 and finishes with the conclusions in chapter 6. As a part of this task, we developed some specific noise models (e.g. the internal LiDAR noise models) and then curated other noise models used for compounding in this report; they are available in the library at: https://github.com/roadview-project/Compound_Noise_Models_Library.

2 Methodology: Noise Factor Analysis

A thorough understanding of the sources of noise affecting a perception sensor is required to firstly understand which effects are required to be modelled and secondly to understand which sources of noise should be compounded to ensure the modelled noise is realistic. WMG has previously defined a framework to break down the noise affecting automotive LiDAR and applied it also for automotive camera [4] [5]. A version of the identified noise factors from these frameworks is presented in Appendix A and Appendix B, more explanation is provided in the published journals and preprint [4] [5] [6].

The noise factor analysis framework, see in Figure 1, is a systematic way of guiding the researcher and user's thinking to identify, breakdown and understand the impact of noise factors. In this framework, the five categories of noise factors based on the p-diagram (i.e. piece to piece, change over time, usage, external environment and system interactions), are considered in the context of an automotive vehicle to determine the different sources of noise (Step 1). Moreover, the format of the sensor data output is determined. Each identified noise factor is then carefully considered to understand which outputs will be affected by the noise (Step 2). One this relation is identified the single noise can be modelled (Step 3) and then combined with other noise factors (Step 4). Finally, the output data can be evaluated (Step 5).

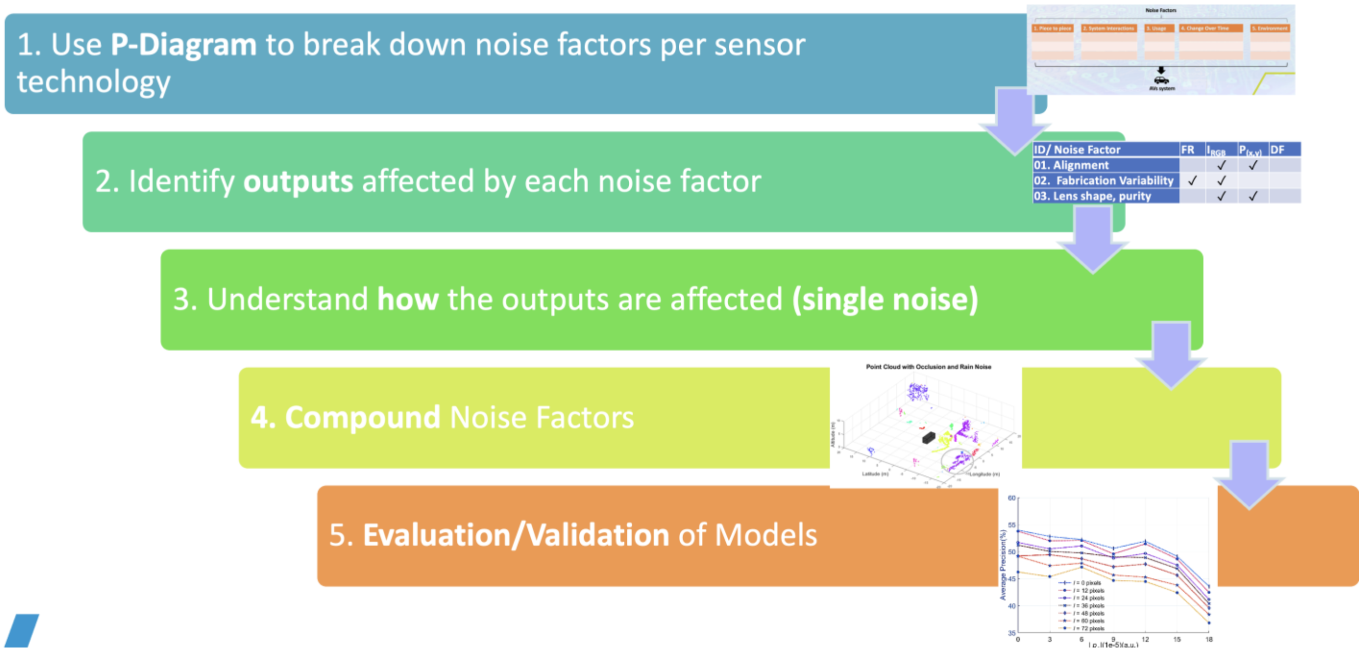

Figure 1: The workflow for the noise factor analysis framework proposed by WMG.

In ROADVIEW T3.5, WMG has extended previous analysis and applied this framework to 4D RADAR. The uniqueness of the 4D RADAR output is that the output data is in the form of a 3D pointcloud with further information of RCS, velocity and power per point. A total of 23 noise factors were identified and broken down on how they affect the 4D RADAR data, Table 1. For each of the identified noise factors, the following properties of the 4D RADAR pointcloud are considered, with a checkmark signifying if the property is affected by the noise:

1. **Location** – the determined three-dimensional point position relative to the 4D RADAR's reference frame. Factors may also affect the **Max Range -** the furthest range from the 4D RADAR which a target can be detected (which can decrease in the presence of noise);
2. **RCS** – the RADAR Cross Section is a processed output based on the target (e.g. size, material properties etc.) and the RADAR (e.g. frequency, incident angles etc.);
3. **Velocity** – The radial velocity of the target relative to the 4D RADAR which can be calculated using the Doppler effect;
4. **Target power** – the reflected power by a target measured by the 4D RADAR for every point (based on factors such as emitted power, RCS, propagation losses, etc.). Along with **Noise Floor** allows the determination of the Signal-to-Noise Ratio (SNR). The noise floor amount of background radio waves which is detected and considered the baseline noise.

Throughout all the noise tables, there are some common noise factors affecting all the sensors. Noise factors are also often observed in conjuncture with other noise, for example obstructions and adverse weather. These tables provide the basis of which the direction for noise modelling development and compounding of model should focus on. In particular, the sources of noise which are difficult to be corrected or mitigated noise (e.g. weather) have been previously deemed to be the most important during workshops with industry experts.

Table 1: A list and breakdown of 4D RADAR noise factors [6].

Factor Type	ID/ Noise Factor	Location (Max Range)	RCS	Velocity	Target power (Noise Floor)
Piece to Piece	01. Alignment of components	(✓)	✓		✓(✓)
	02. Fabrication Variability	✓(✓)	✓	✓	✓(✓)
	03. Radome	✓(✓)	✓		✓
	04. Signal Processing	✓(✓)	✓	✓	✓
Change over Time	05. Ageing of electronics + Si	✓(✓)	✓	✓	✓(✓)
	06. Misalignment of SoC with Radome	✓(✓)	✓		✓
	07. Degradation of Radome		✓		✓
Usage	08. Misplacement of Sensor	✓(✓)			✓
	09.Vehicle Impact	✓(✓)	✓		✓(✓)
	10. Chemicals, contaminant, component damage	✓(✓)	✓		✓(✓)
	11. Obstructions	✓(✓)	✓		✓(✓)
	12. Vehicle Dynamic Settings	✓(✓)			✓(✓)
	13. Firmware, Memory, Software corruption	✓(✓)	✓	✓	
	14. Emitted Frequency	✓(✓)		✓	✓(✓)
	15. Internal Component Noise	✓	✓		✓(✓)
Environment	16. Extreme Temperature	✓(✓)	✓	✓	✓(✓)
	17. Adverse Weather	✓(✓)	✓	✓	✓(✓)
	18. Object Clutter	✓	✓	✓	✓(✓)
	19. Multipath Reflection	✓(✓)	✓	✓	✓(✓)
System Interactions	20. Vehicle Bodywork (bumper)	✓(✓)	✓		✓
	21. Power Supply		✓(✓)	✓	✓
	22. Internal Electromagnetic Interference	✓	✓	✓	✓(✓)
	23. Cross Device Interference	✓(✓)	✓	✓	✓(✓)

3 Methodology: compounding of noise factors

The process of a perception sensor sampling and measuring the real-world before producing an output data frame consist of many different steps. Different sources of noise will impact different steps, from the real-world affecting the electromagnetic waves' propagation, to the introduction of noise during signal detection and processing to produce the final output. In an automotive context, it is unlikely for the sensor to be only affected by one source of noise. To ensure that the multiple noise models are correctly applied concurrently, an understanding is needed into when the noise is introduced into the capturing process. Depending on this aspect, and the specific effect of each noise factor on the sensor output, the noise models can be performed sequentially, or they may require a specific model including both noise factors if their occurrence cannot be separated out, see Figure 2.

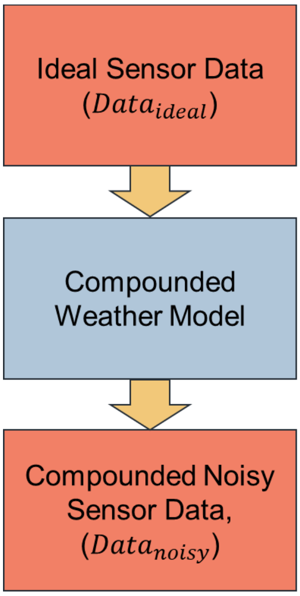

$$\begin{cases} Carla \\ Carmaker \\ Dataset \\ Perception\ Sensor \end{cases}$$

$$\begin{cases} Data_{noisy} = f_{weather}\left(\left(f_{noise}(Data_{ideal})\right)\right) & (1) \\ Data_{noisy} = f_{weather,noise}\left(Data_{ideal}\right) & (2) \\ Data_{noisy} = f_{noise}\left(\left(f_{weather}(Data_{ideal})\right)\right) & (3) \end{cases}$$

Figure 2: Different methodology to apply multiple sources of noise.

Similar to the noise models from D3.4, the input to the compounding noise modelling are also ideal frame data from the sensor. This data can be obtained directly from simulation software such as CARLA and Carmaker or be obtained from real world datasets and live from sensors. However, depending on the format of the initial data, pre-conditioning may be performed to ensure correct format for the models.

In the core block of the compounding weather model, one of three processes will need to be selected for the compounding method:

1. Application of noise onto frame, and the weather model is applied to this output – Eq. (1).
2. Adapting and creating a bespoke model for the combined effect of the two models – Eq. (2).
3. Application of weather model to the input frame, then application of secondary noise model – Eq. (3)

Method 1 and 3 are simple methods, but it is important to ensure the order of application is correct. Figure 3 provides an example for camera on the breakdown of different locations where noise could be introduced in the sensor data up to the perception step. By understanding which part of this pipeline the noise is introduced, the compounding method can be selected appropriately. Adverse weather affects the free space part of the environment, and any noise acting before this or after this is applied using steps one and three respectively. However, additional considerations will need to be understood as the noise factor may require an update to some parameters in the adverse weather model such as the luminosity of the scene. As the focus of ROADVIEW is adverse weather, the physics-based weather models created from T3.4 were chosen for compounding with other noise models. The compounding methodology was implemented using ROADVIEW virtual environment, based on CARLA simulator, used also in WP7. In WP7, a mixture of virtual and real-world testing is performed to test the ROADVIEW system in adverse weather. The hereby proposed compounding framework and library can be used to support the generation of compounded conditions in CARLA for XiL testing in WP7.

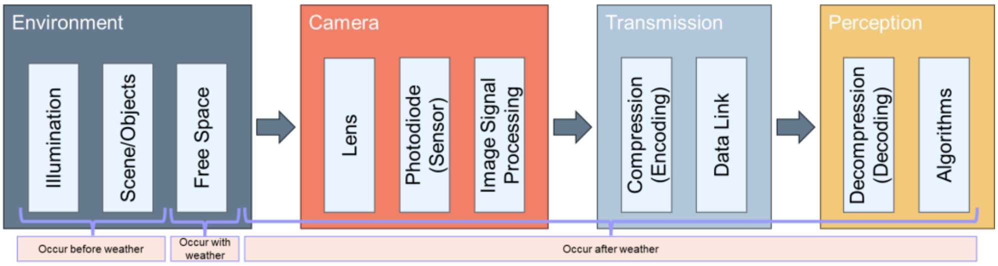

Figure 3: Example of the information flow from environment though a perception sensor to the downstream perception task of an automated system.

Based on the noise factor analysis of perception sensors presented in chapter 2, a list of noise factors, Table 2, are explored as a part of this task. Several models, including the internal LiDAR noise models have been created as part of T3.5. Other models are based on previous models or based on existing functions within the opencv computer vision library. The model codes are available in the published ROADVIEW GitHub library.

Each one of the noise factors in Table 2 have been compounded against the three ROADVIEW weather models (rain, fog and snow) from T3.4 to form a total of 30 compounded noise models [3]. The used compounding method and the resulting noisy sensor data are presented in Chapter 5.

Table 2: List of noise factors for compounding and the source of the model.

Noise Factor	Sensor	Source
Laser Alignment Error	LiDAR	New ROADVIEW model (Chapter 4)
Laser Power Variance	LiDAR	New ROADVIEW model (Chapter 4)
Occlusion	LiDAR/4D RADAR	New ROADVIEW model (Chapter 5.2.3)
Wind	Camera	New ROADVIEW model (Chapter 5.1.6)
Lens Soiling	Camera	New ROADVIEW model (Chapter 5.1.1) **[7]**
Windscreen Distortion	Camera	New ROADVIEW model (Chapter 5.1.2) **[5]**
Motion Blur	Camera	Adapted from Opencv library functions (remap, addWeighted) (Chapter 5.1.3) **[8]**
Lossy Compression	Camera	Adapted from Opencv library functions (imencode) (Chapter 5.1.4) **[8]**
Low Light	Camera	New ROADVIEW model based on cycleGAN (Chapter 5.1.5) **[9]**
Ray Drop	LiDAR	WMG machine learning model adapted for ROADVIEW (Chapter 5.2.4) **[10]**

4 Data driven internal LiDAR noise models

In this work, the rotating multi-beam LIDAR Velodyne Alpha Prime (VLS-128) is studied to form a model of its internal measurement geometry and to model its response to objects of different reflectance. First the sensor is calibrated using a simplified two-parameter geometric calibration model for each LIDAR beam. Each laser emitter receiver pair, i.e. beam, is assumed to measure the range and the reflected intensity of the emitted pulse according to the manufacturer specifications. In this simplified model, the alignment of the receiver-emitter system is defined with two parameters (azimuth α_i and elevation ω_i for each laser beam $i \in [1,128]$) and their values are initially set according to manufacturer given calibration table (see page 72 in [11]).

4.1 Geometric calibration

The sensor data is commonly used as a 3-D point cloud consisting of points which all have Cartesian coordinate x, y, and z associated with an intensity value. The sensor driver computes the Cartesian coordinates from the azimuth and elevation parameters, and a motor rotation angle α_m and a laser range measurement r_i for each i using the following equations (see page 59 in [11]):

$$
\begin{aligned}
x_i &= \cos(\omega_i)\sin(\alpha_m + \alpha_i)\, r_i \\
y_i &= \cos(\omega_i)\cos(\alpha_m + \alpha_i)\, r_i \\
z_i &= \sin(\omega_i)\, r_i
\end{aligned}
\tag{4}
$$

The variation of elevation ω_i and azimuth α_i angles to the manufacturer specified values are measured by calibrating these elevation and azimuth parameters for each laser emitter and receiver pair using a static scene on a rotating platform (see Figure 4 A) to allow same LIDAR beams to measure same locations around the room which contains planar wall and floor sections in all directions (See Figure 4 B). The parameters are tuned to minimize the variation in normal direction for each plane using Matlab's fminsearch function, which uses Nelder-Mead Simplex method [12]. The parameter minimization is repeated 60 times with different data samples collected with varying angular velocities of the rotating calibration platform in the same room.

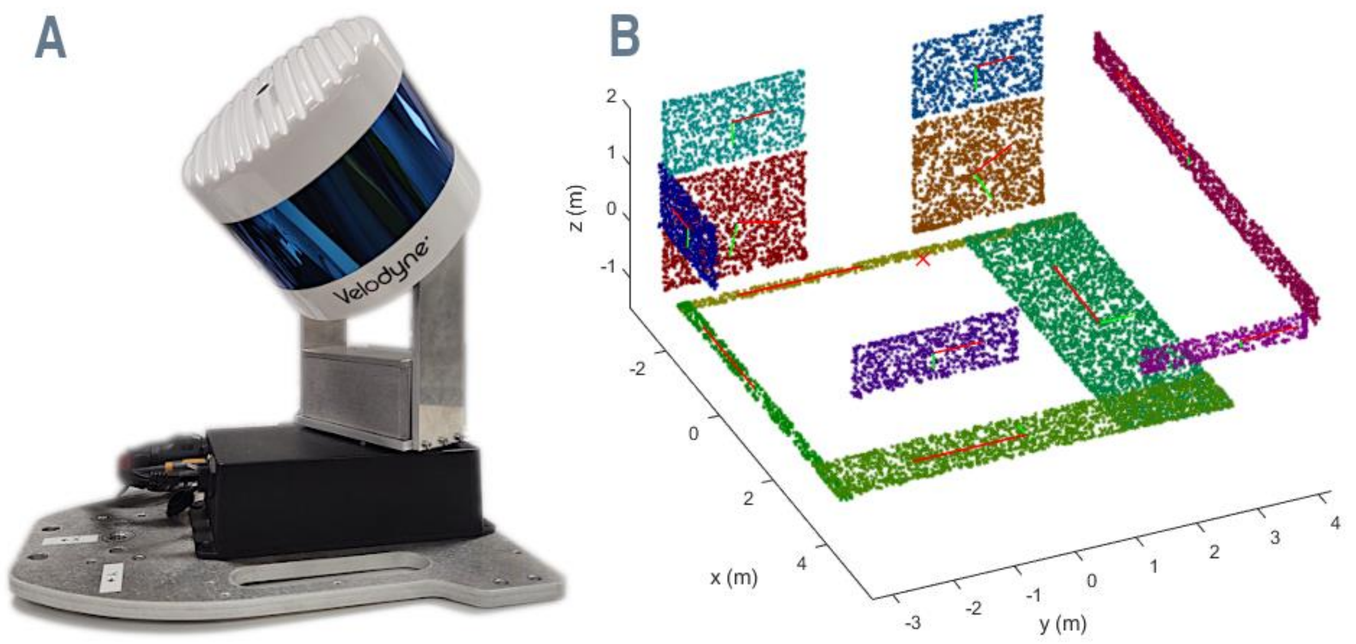

Figure 4: A) calibration platform with the Velodyne Alpha Prime (VLS-128) sensor mounted on top. B) The calibration room with the point clouds of the extracted planes used for calibration shown in different colours.

Average parameter values (α_i and ω_i for each i) are used as calibrated parameter values for each LIDAR beam to form a sharper 3-D point cloud. The differences of manufacturer reported default parameters, and the calibrated parameters have been collected as a histogram (shown in Figure 5 below) to model the statistical deviation of the beam angles from the manufacturer reported calibration parameters. As shown in the image, the elevation angle deviates significantly more than the azimuth angle. A normal distribution has been fitted on top of the histograms to model the average variation in these parameters for building a noise model later.

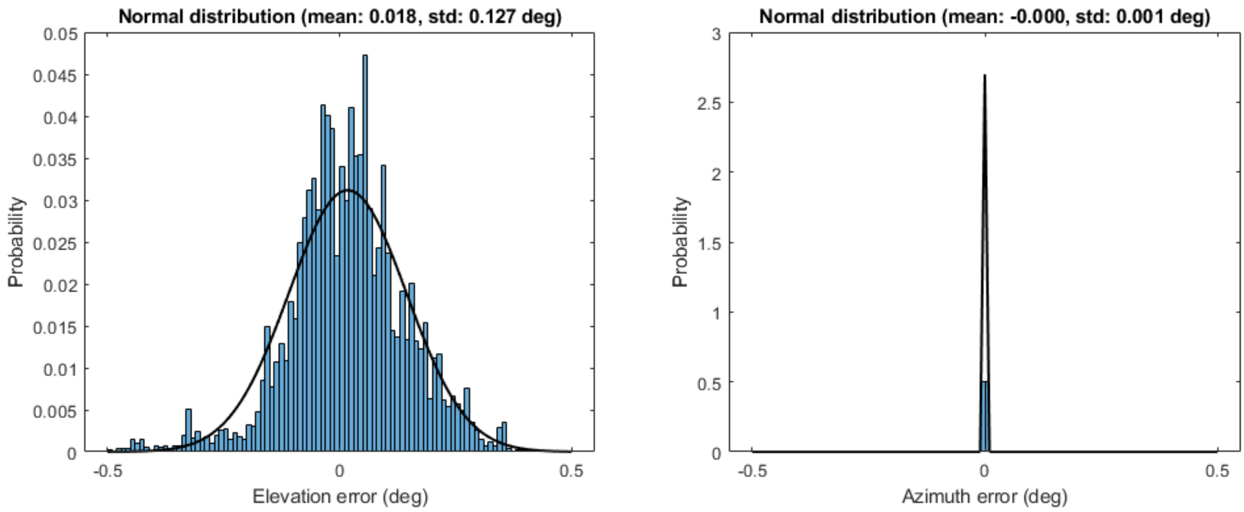

Figure 5: Measured calibration errors in the manufacturer reported calibration values for elevation and azimuth angles for the selected Velodyne Alpha Prime (VLS-128) sensor. The black curve on top of the statistics histogram is the fitted normal distribution.

4.2 Radiometric calibration

The radiometric response of each LIDAR beam has been measured using reflectance calibration plates reflecting 1) 10%, 2) 20%, 3) 40%, 4) 80%, and 5) 99% of the incoming light (see Figure 6). Also, a picture of the setup is shown in Figure 6 B.

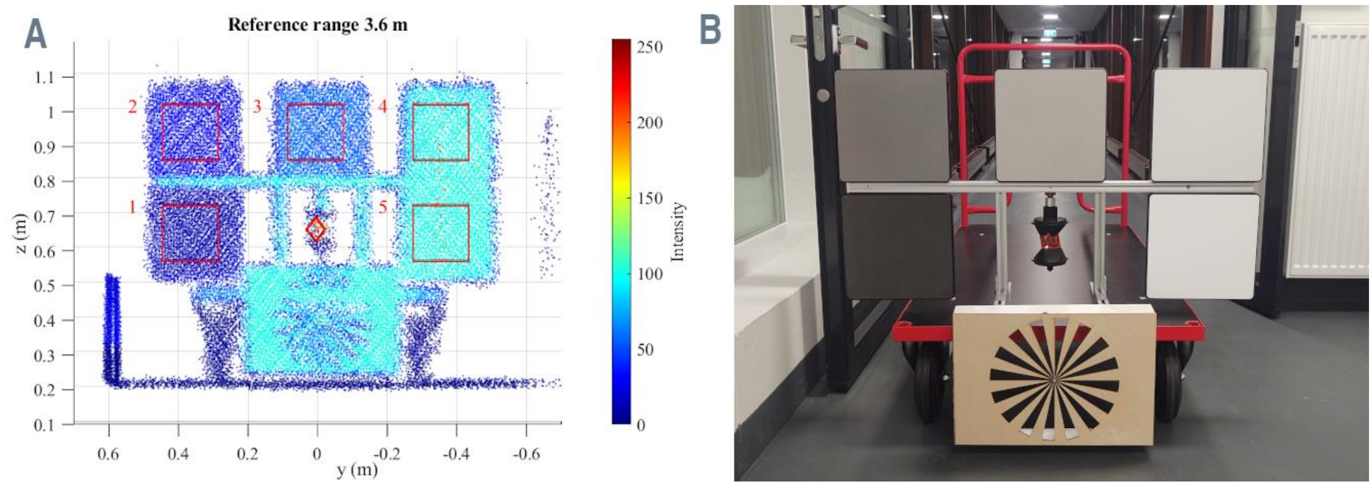

Figure 6: A) A measured point cloud using the rotating platform shown in Figure 4 A at the distance of 3.6 meters from the LIDAR. The 5 calibration plates and the bounding boxes used for selecting points for measuring the intensity response related to each of the calibration plates are drawn in red on top of the point cloud. B) Intensity calibration platform with reference positioning prism located at the centre, and the 5 intensity calibration plates placed around it.

Each beam of the LIDAR emits a laser pulse, waits for a reflected echo, and measures the power of the returning light pulse. The power of the returning light is reported as an intensity value (8-bit unsigned integer). The average intensity response from plates 1 to 5 at different distances from the scanner is visualised in Figure 7 below. As seen in the figure, two of the brightest plates are overlapping and their values are capped to 100. Furthermore, some of the measurements from the plates 4 and 5 are forming a comb-like pattern at intensity values a lot larger than 100. Only three lower reflectivity plates (1-3) are separated better, and the distribution of their responses are closer to a normal distribution.

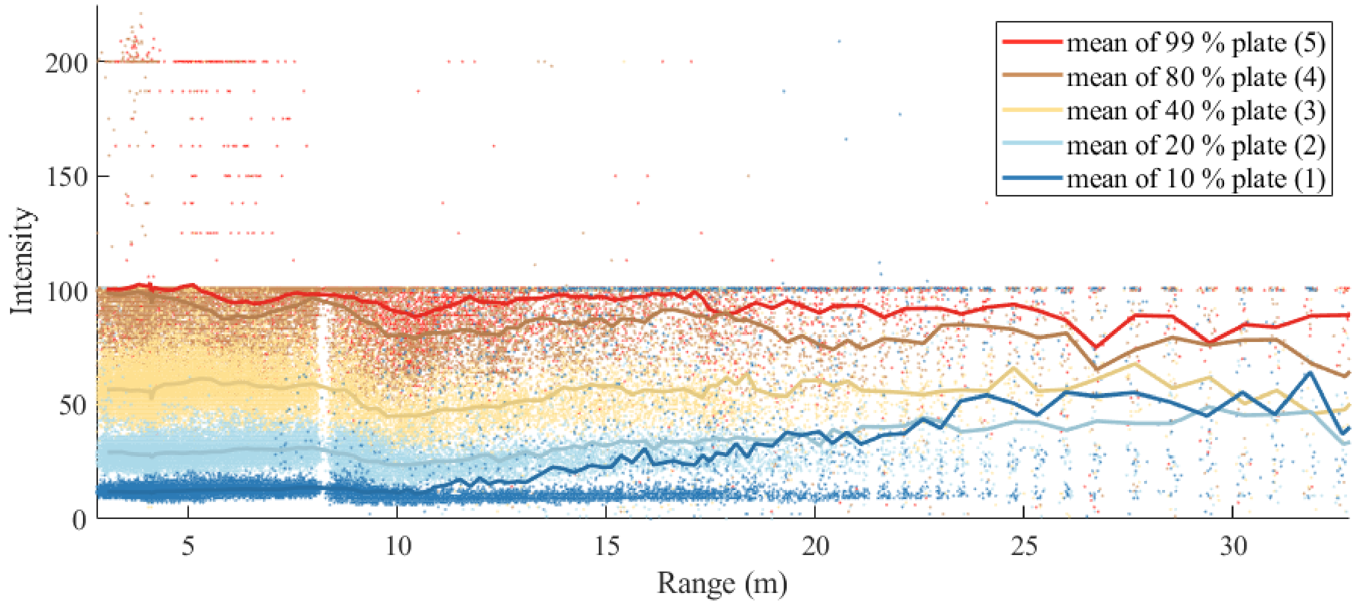

Figure 7: All measured intensity responses of LIDAR measurements hit into intensity calibration plates 1 to 5, and their mean values. The test is made up to 71 meters, but on 30 first meters are shown since after 20 meters the random intensity values start to dominate the distribution and the means tend to merge at the middle.

The intensity is modelled as normally distributed noise around the mean value. This analysis is done only for the four lowest (1-4) reflectivity plates and to the first 10 meters where the random noise (increases from left to right in Figure 7) was substantially low.

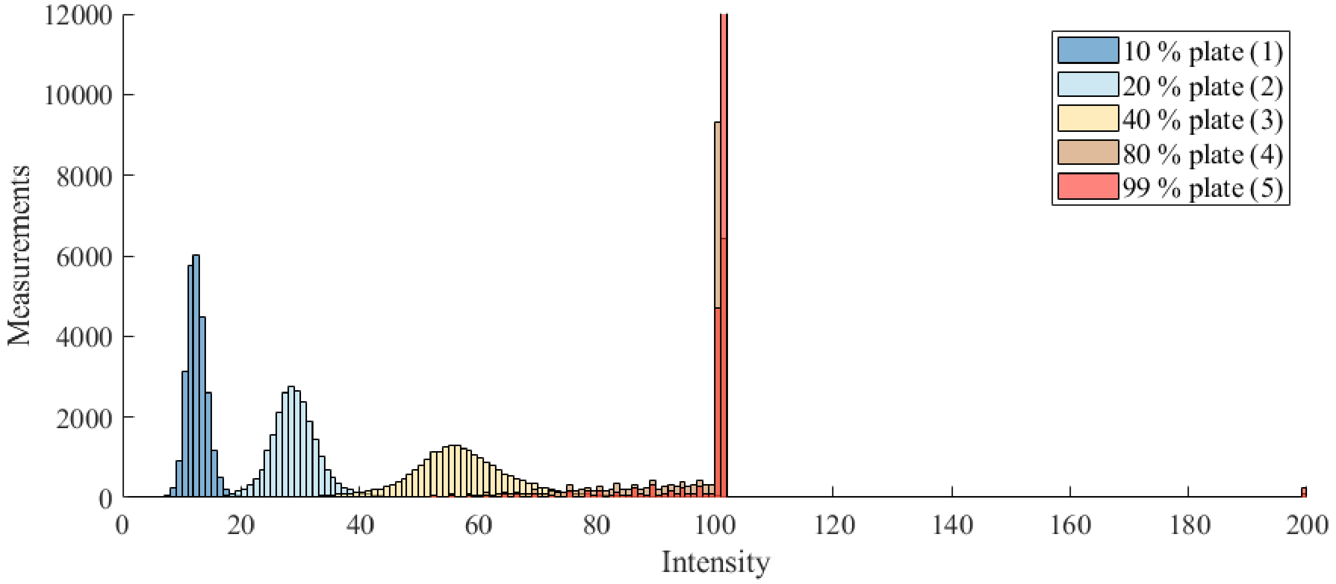

Figure 8: Histograms of all measurements at the first 10 meters from plates 1 to 5.

The 99 % reflectivity plate gave a lot of intensity measurements near 200 (see Figure 7) so it does not hold with the assumption of normally distributed response (see also histograms in Figure 8). There might be some internal logic in the sensor for detecting retroreflective objects, which could have caused this kind of nonlinear behaviour of the intensity measurement. This should be managed with another model in the future work. Here these measurements are omitted. Similarly, the 80% reflectivity plate gave some significantly large intensity values, and its response is also not normally distributed as it can be seen from Figure 8. However, we decided to include the 80% plate into the modelling.

The average intensity values and standard deviations of the intensities over all data from the first 10 meters for the plates 1-4 are shown in the following Table 3. As it can be noted, the standard deviation increases linearly with the mean.

Table 3: Mean values of the intensity measurements at first 10 meters for plates 1 to 4.

	10% plate (1)	20% plate (2)	40% plate (3)	80% plate (4)
Number of measurements	25372	24378	23600	24779
Mean intensity	12.14	28.77	57.13	94.66
Standard deviation of intensity	2.63	4.95	9.73	13.69

Next, the laser range measurements hitting plates 1-4 are analysed to tune a calibration model for the intensity response of each LIDAR beam. The used data is shown in Figure 9 below. The data for first 10 meters is quite normally distributed, does not depend much on range, and each plate is easily distinguishable.

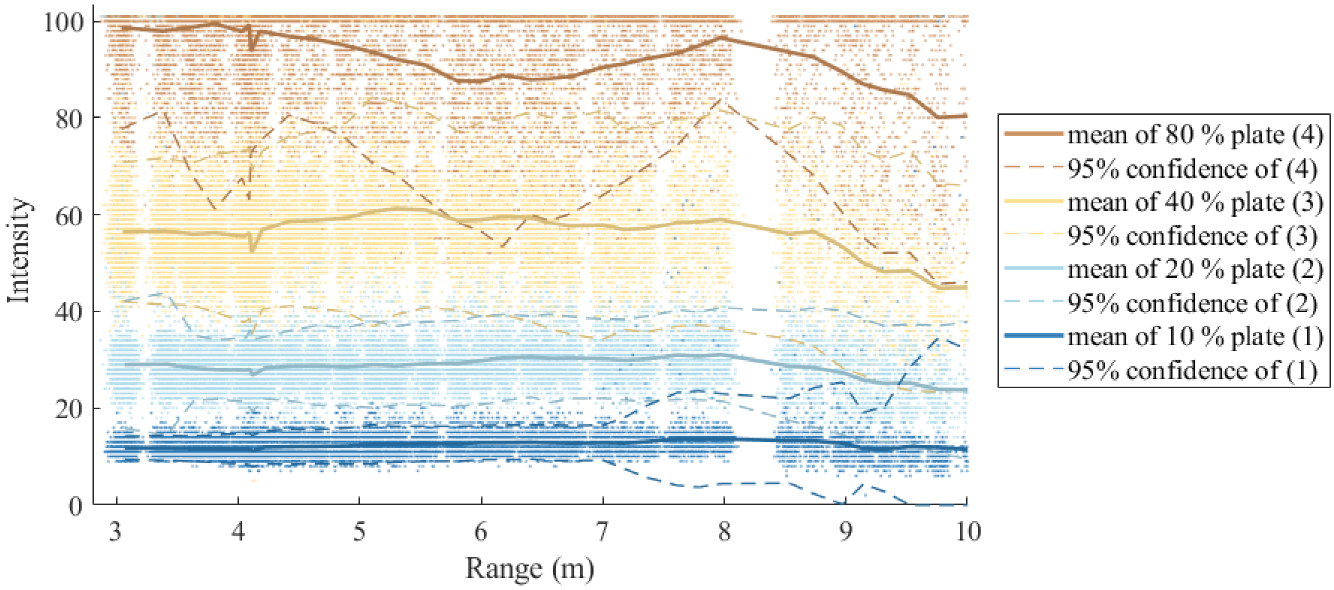

Figure 9: The measurements from the reflectivity plates 1-4 at the first 10 meters with associated means and 95% confidence intervals.

Because of the use of the rotating platform allowing all beams to observe all reflectance plates, the same intensity response seen in Figure 9 can also be plotted for each LIDAR beam i separately. It is shown in Figure 10 below. A mean value for each plate and for each LIDAR beam is drawn as a line on top of the scatterplot. Each LIDAR beam has got on average around 190 measurements from each plate (see more elaborated statistics in Table 4).

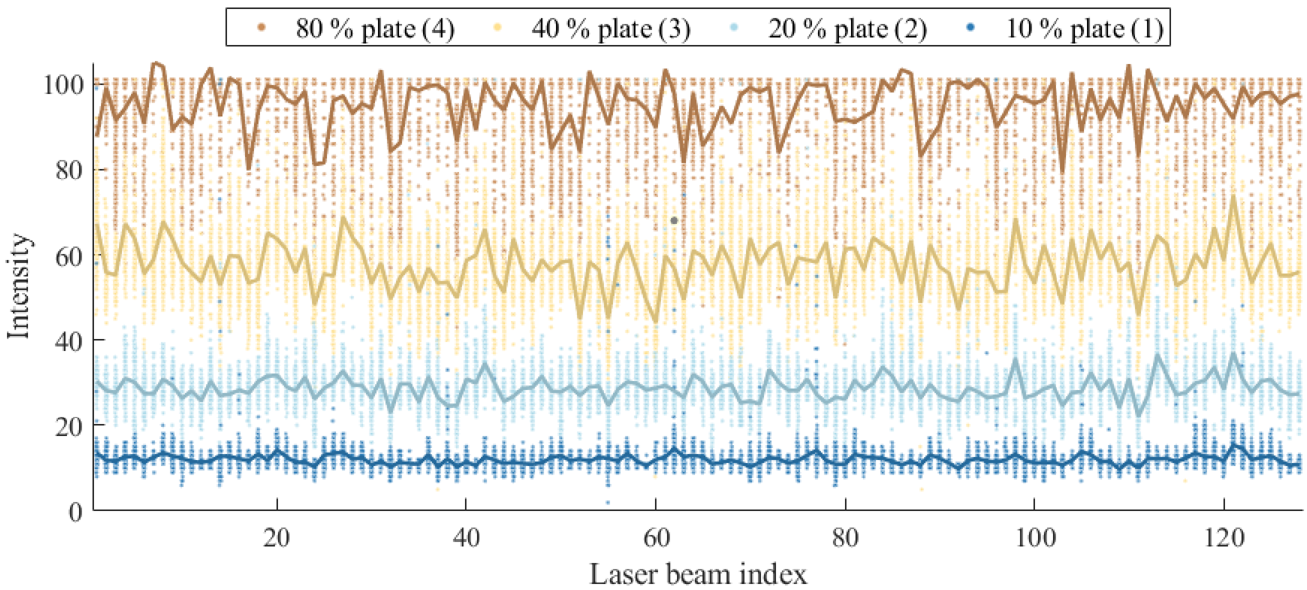

Figure 10: The measurements coming from the reflectivity plates 1-4 from the first 10 meters are plotted as a function of laser beam index. Also means are drawn on top of the distributions as solid lines.

Table 4: Statistics of individual laser beam measurements at first 10 meters for plates 1 to 4.

	10% plate (1)	20% plate (2)	40% plate (3)	80% plate (4)
Total number of measurements	25372	24378	23600	24779
Minimum number of measurements from a laser beam	41	113	103	88
Average number of measurements from a laser beam	198.2	190.5	184.4	193.6
Maximum number of measurements from a laser beam	403	288	346	388

As it can be seen from Figure 10, most LIDAR measurements associated to individual beams have similar low-noise behaviour especially when reflectivity of the target is low. It should be noted that in the data coming from the more reflective plates, there are quite large differences between beams. This suggests that some LIDAR beams either produce more light power to the target or alternatively their receivers are more sensitive to the echoed and returning light pulse.

To compensate for these differences, each of the LIDAR beam is calibrated using a linear model for the intensity reply using measurements from the reflectance plates 1 to 4. The linear model is the following,

$$y = gain \cdot x + bias \,, \tag{5}$$

in which x is the true reflectance value multiplied by a gain and then a bias is added to form the measured intensity value y. The parameters gain and bias are estimated separately for all the 128 LIDAR beams and shown as a distribution in Figure 11.

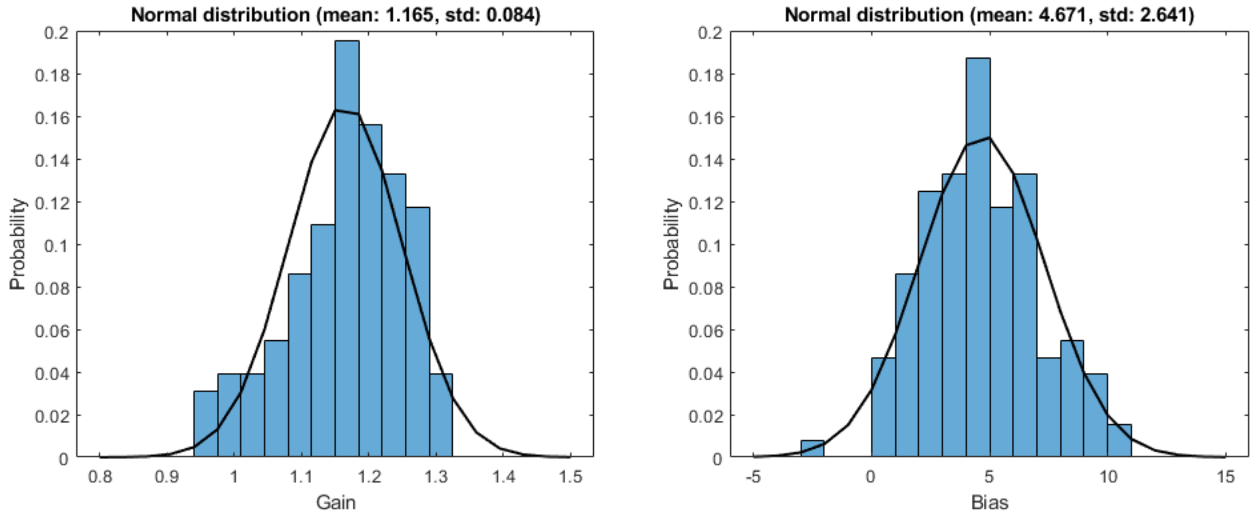

Figure 11: Probabilities of the found gain and bias parameters for all LIDAR beams. They are quite normally distributed, gain parameter having a mean of 1.17 and standard deviation of 0.084, whereas bias has a mean of 4.67 and standard deviation of 2.64.

After the compensating the measured intensity values by the model in Eq. (5) and the found bias and gain parameters, the mean values of plate intensities drift closer to the reflectance value of each calibration plate and differences between LIDAR beams reduce as seen in Figure 12.

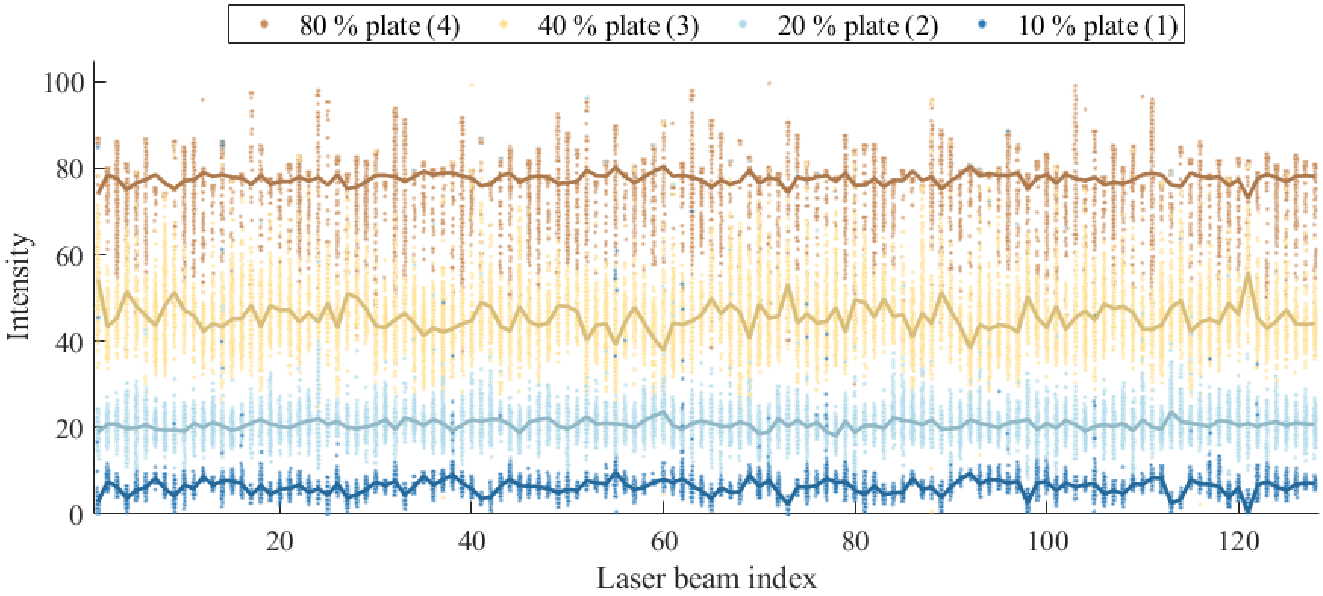

Figure 12: The corrected measurements coming from the reflectivity plates 1-4 from the first 10 meters are plotted as a function of laser beam index. Also means are drawn on top of the distributions as solid lines.

The mean values over all data from the first 10 meters for each plate after the correction based on the calibration are listed in Table 5. As it can be noted, the linear model did not correct the data perfectly, the mean of the 10% and 80% reflectance plates are falling under the target and 40% plate is seen larger than the target reflectance. In the future work, some more sophisticated nonlinear calibration model should be used instead. However, the current model already improves the result significantly.

Table 5: Mean values of the intensity measurements at first 10 meters after the correction.

	10% plate (1)	20% plate (2)	40% plate (3)	80% plate (4)
Mean intensity after correction	6.08	20.78	45.13	77.37

4.3 The noise models

In this part, the previous calibration results are used to simulate similar distortions for perfect 3D data than if the data would have been produced by scanning with similar mechanically rotating LIDAR sensor. For geometric calibration part, the non-ideal formation of 3D point cloud caused by erroneous azimuth and elevation calibration parameters is modelled next as a noise model for internal geometric calibration.

The noise model for internal LIDAR geometric calibration is defined as constant random parameters sampled from the measured variance for LIDAR beams in elevation and azimuth direction. The noise parameters are defined according to the average measurements and the geometric calibration process. We simply used mean and standard deviation of distribution of differences in elevation and azimuth angles compared to the manufacturer given default parameters. We assume that similar rotating sensors from the same manufacturer should have similar statistical properties on their elevation and azimuth angles of the laser beams.

To apply the geometric LIDAR noise model, the point cloud needs to lie in spherical sensor-centric coordinates (range r, elevation ω, and azimuth α angles) defined by the manufacturer manual [11]. If the input point cloud is provided in Cartesian coordinates (i.e., as xyzi point cloud), it needs to be transformed into spherical sensor-centric coordinates. This can be computed by inverse of the LIDAR internal geometric model in Eq. (4):

$$\begin{aligned} r &= \sqrt{x^2+y^2+z^2}, \\ \alpha &= \operatorname{atan2}(x,y), \\ \omega &= \operatorname{atan2}\left(z,\sqrt{x^2+y^2}\right), \end{aligned} \tag{6}$$

which assumes that the origin is at the optical centre of the LIDAR sensor. Since each LIDAR beam has a unique ω, it can be used to distinguish the correct LIDAR index i of each measurement in the 3-D point cloud. In the model, each LIDAR beam has its own noise characteristics, sampled once for the simulated sensor and recorded with the associated LIDAR index i, the noise can now be applied into all measurements such that noise for each i shares the same distortion.

In practice, when applying the geometric noise model, the elevation and azimuth angles are incremented with the LIDAR beam associated offsets and then Eq. (4) is used to bring the data back into Cartesian coordinates.

The noise model for the power variance i.e., the variance in the intensity response of the LIDAR sensor, is also based on the real measurements using the reflectance plates and the calibration measurements described earlier. Similarly to the geometric model, in the laser power noise model, first a bias and a gain parameter is sampled once from the measured normal distributions (see Figure 11) for each LIDAR beam and saved for future use. This sampled bias and gain parameter is used with Eq. (5) to produce distorted intensity response for all measurements as a function of the related laser beam index i.

In addition, in the reflectance calibration, we noted that the standard deviation of the intensity response increases with the mean value (see Figure 8). A random noise can be applied after the noise model for the power variance into the intensity values with a standard deviation of 0.14 * intensity to produce similarly increasing noise for the signal than what was observed with the data captured for this work.

5 Compounding Models

A series of noise models was explored for the different sensor modalities, which could be compounded with each of the three physics-based weather noise models developed in task 3.4 for each one of the perception sensors, i.e. camera, LiDAR and 4D RADAR. Table 6 presents the list of the selected compounded noise models combined, for a total of 30 different compounded models. The reasons for selecting each additional Noise factor are explained in the following sections.

Table 6: List of 30 compounded noise factors for ROADVIEW with the weather models from WP3, with their unique identifier the Compound Noise Factor (CNF) Index.

CNF Index	Sensor	Additional Noise Factor	Weather Noise Factors (T3.4)	Compound Method (Equation no.)
CNF1	Camera	Lens Soiling	Rain	Occurs **After** Weather **(3)**
CNF2			Fog	
CNF3			Snow	
CNF4	Camera	Windscreen Distortion	Rain	Occurs **After** Weather **(3)**
CNF5			Fog	
CNF6			Snow	
CNF7	Camera	Motion Blur	Rain	Occurs **After** Weather **(3)**
CNF8			Fog	
CNF9			Snow	
CNF10	Camera	Lossy Compression	Rain	Occurs **After** Weather **(3)**
CNF11			Fog	
CNF12			Snow	
CNF13	Camera	Low Light	Rain	Occurs **Before** Weather **(1)**
CNF14			Fog	
CNF15			Snow	
CNF16	Camera	Wind (ROADVIEW Model)	Rain	Occurs **With** Weather **(2)**
CNF17			Fog	
CNF18			Snow	
CNF19	LIDAR	Laser Alignment Error (ROADVIEW Model)	Rain	Occurs **Before** Weather **(1)**
CNF20			Fog	
CNF21			Snow	
CNF22	LIDAR	Laser power variance (ROADVIEW Model)	Rain	Occurs **Before** Weather **(1)**
CNF23			Fog	
CNF24			Snow	
CNF25	LIDAR 4D RADAR	Occlusion (ROADVIEW Model)	Rain	Occurs **After** Weather **(3)**
CNF26			Fog	
CNF27			Snow	
CNF28	LiDAR	Ray Drop	Rain	Occurs **Before** Weather **(1)**
CNF29			Fog	
CNF30			Snow	

5.1 Camera Compounded Noise Factors

Table 6 presets 6 camera noise factors with the models coming from different sources. This subsection presents the model and the compounded images when applying both the weather and the noise factor. The compounding method have been applied using the pre-processed ideal frame, Figure 13, as the input frame.

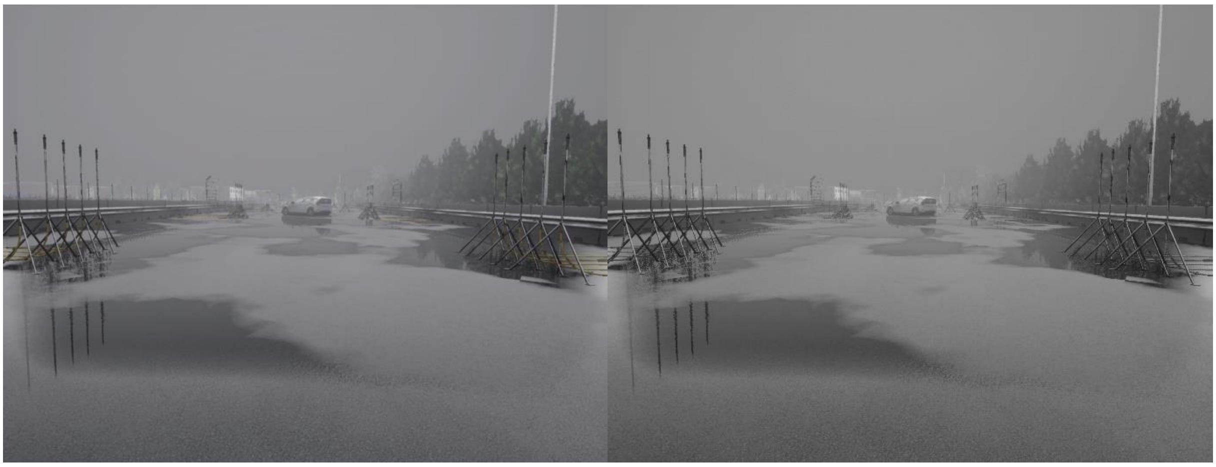

Figure 13: A frame generated in CARLA using the ROADVIEW digital twin used as the ideal input frame for this work. Left: Original frame. Right: Bayerised (pre-processed) ideal frame.

For the best effects based on the scene, the following rates were set for the weather models: rain at 50 mmh^{-1}, fog at 30 m visibility, and snow at 3.03 mmh^{-1}, see Figure 14 [3].

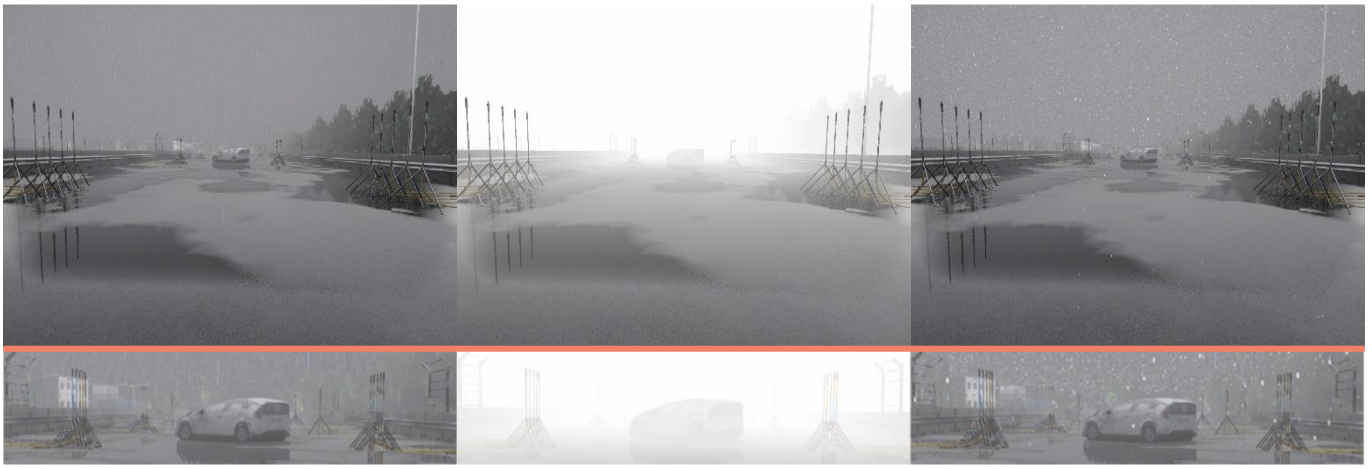

Figure 14: Noisy images generated using the defined weather rates for compounding. Left: Rain. Middle: Fog. Right: Snow. Bottom is a zoomed in region of the image.

5.1.1 Lens Soiling and Rain, Fog, and Snow (CNF 1, 2, 3)

Lens soiling from mud is an important aspect to understand for AAD as it can occur simply by driving behind another vehicle which flicks mud backwards from the wheels, especially when the ground is wet. We previously presented an obstruction model for automotive camera [5], and further improved the rendering of the model for ROADVIEW in [7]. The model is an empirical model based on the observed effects from the Uřičář et al.'s dataset on mud-obstructed images [13]. Using the obstruction model as a mask (see Figure 15), the obstruction is applied sequentially after the application of the weather, see Figure 16. The high occlusion intensity was generated using the parameters $S_{\{min\}}$, $S_{\{max\}}$ and $Intensity$ values of 93, 271, and 0.45 respectively.

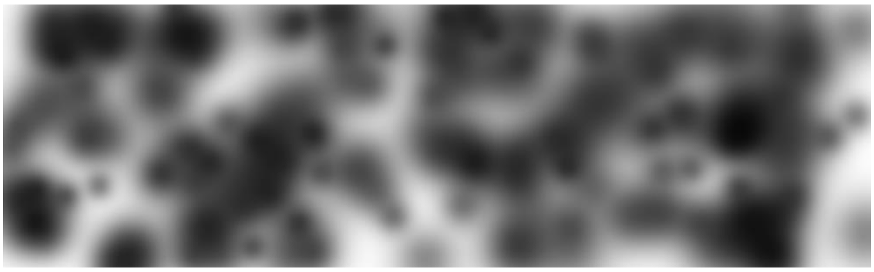

Figure 15: An occlusion mask classified as high intensity generated in Baris et al. for occlusion-weather compounding [7].

The occlusion model stands out the most when compounding with weather. It is observed that there will be areas which have high impact, especially if there are clusters of occlusions that is observed in the bottom right. These areas will make it difficult to detect objects covered by that area. When combined fog, it can become even more challenging as the patch of occlusion creates a gradient effect across the target vehicle and this could make it more difficult for an algorithm to detect.

Figure 16: Weather model compounded with a lens soiling model. Left: Rain. Middle: Fog. Right: Snow. Middle row: zoomed in area of the frame. Bottom row, corresponding zoomed area in the original image.

5.1.2 Windscreen Distortion and Rain, Fog and Snow (CNF 4, 5, 6)

Front facing cameras to support different AAD functions are often placed within the vehicle behind the windscreen, and in this case the curvature of the vehicle windscreen can cause a distortion to the image and cannot be fully compensated for. To model windscreen distortion, we proposed a parametric model based upon the Brown-Conrady Polynomial (BCP) distortion model, with a focus towards adding tangential distortion [5]. As the distortion happens after the light propagates to the sensor, but before the signal is detected, our distortion model was applied sequentially after the weather model for compounding, see Figure 17. The BCP parameter of K_1 parameter was set as 0.0000001, with the other parameters as 0 based on the visually created distortition.

Based on the selected model parameters, there is drastically more distortion of the frame content around the edge of the image. For example, this effect is evident by the curvature of the sprinkler pole. Overall, the distortion does not interact significantly with the weather noise models. The appearance of the noise for fog is unaltered, but with the distortion of the frame described above due to the windscreen. However, for rain and even snow, where streaking occurs, there streaks might appear as curved accordingly to the windscreen distortion.

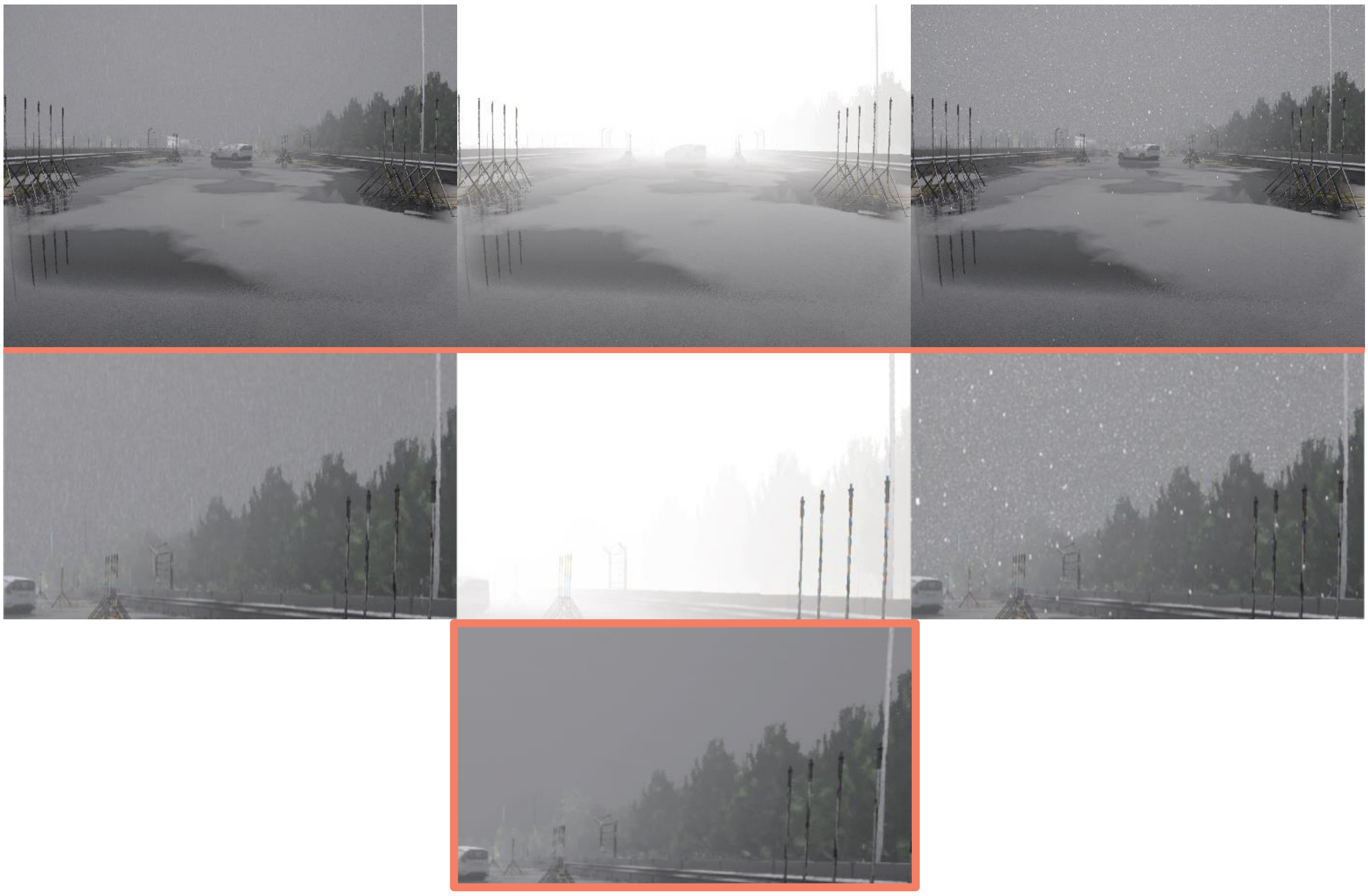

Figure 17: Weather model compounded with a windscreen distortion model. Left: Rain. Middle: Fog. Right: Snow. Middle row: zoomed in area of the frame. Bottom row, corresponding zoomed area in the original image.

5.1.3 Motion Blur and Rain, Fog and Snow (CNF 7, 8, 9)

The field of view (FoV) of the camera results in a disproportionate relative speed at which objects pass depending on their position in the FoV. Motion blur can have different effects on the image based on the pose of the mounted camera and the direction of travel. In this compounding methodology model, it is assumed that the camera pose is aligned with the direction of travel (i.e. front facing camera). In this case, objects towards the edge appear as they were moving at a higher relative speed, resulting in a radial blur of the content of the pixels. A widely deployed blurring algorithm from the python openCV library was selected, with the blur intensity increasing based on the distance from the image centre. Motion blur is a phenomenon due to how the light is captured within the sensor chip and hence applied sequentially after the weather noise for compounding, Figure 18. Based on the created effects, the $blur$ parameter and $interation$ parameters were defined as 0.002 and 7 respectively.

The effect of motion blur is progressively stronger towards the edge of the frame if the camera is pointed directly at the direction of travel. As with windscreen distortion, fog noise was relatively unaffected by motion blur. Conversely, for rain and snow, it is seen that the rain streaks and snow appear blurred and weaker under the heavier effects of motion blur (the periphery of the image).

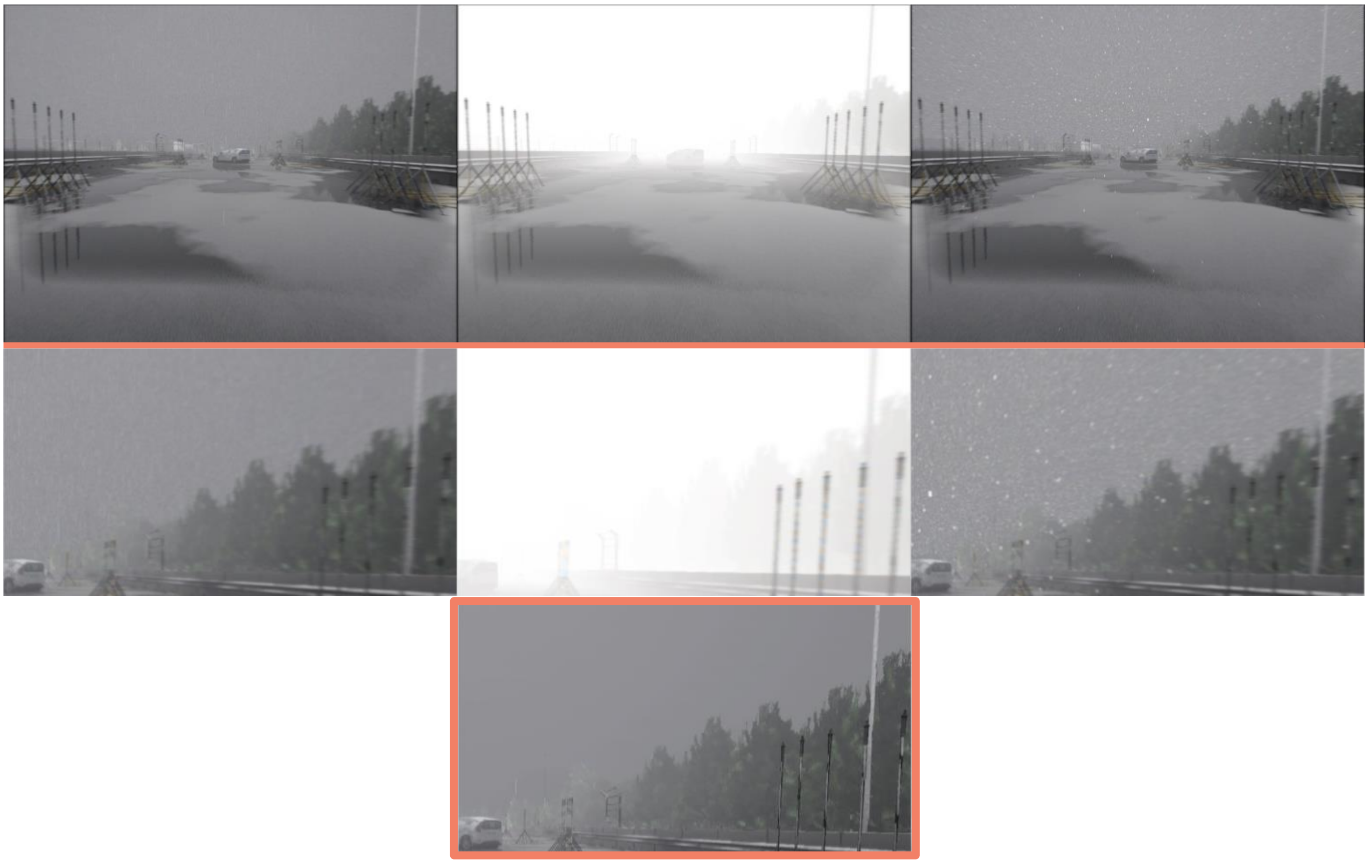

Figure 18: Weather model compounded with a motion blur model. Left: Rain. Middle: Fog. Right: Snow. Middle row: zoomed in area of the frame. Bottom row, corresponding zoomed area in the original image.

5.1.4 Lossy Compression and Rain, Fog and Snow (CNF 10, 11, 12)

The amount of data produced by an automotive camera sensor can be tremendous. The raw amount of data produced by modern automotive camera can easily exceed 1 Gbps, due to the high resolution and high dynamic range required, and the produced data rate is higher the bandwidth of traditional wired automotive networks and even the gigabit automotive ethernet standard. Coupled with the need for multiple camera sensors to properly support AAD functions, it is expected that lossy compression may play a role to support the vehicle's bandwidth requirements. Previous works have demonstrated that, up to a certain amount, lossy compression does not affect the overall performance when detecting vehicles in compressed camera frames [14]. For ROADVIEW, the python openCV library function imencode was used to implement lossy JPEG compression. Within a sensor, compression would happen after the data is fully captured, hence is applied after the weather for compounding, see Figure 19.

Under heavy compression (~125:1, 142:1, 104:1 compression ratio using a $quality$ parameter of 15 for rain, fog and snow respectively) many artifacts are generated when compounding. Compared to previous models where the vehicle was still identifiable under fog, the compression combined with the decrease of contrast of the fog has caused severe banding and blocking artifacts. The blocking also drastically reduces the resolution of the vehicle, and other details in the image. For rain and fog, the effect of the compression and in particular block changes the shape and appearance of the streaks and snow particles, so they might affect certain objects depending on their streak position and intensity.

Figure 19: Weather model compounded with lossy compression. Left: Rain. Middle: Fog. Right: Snow, Middle row: zoomed in area of the frame. Bottom row, corresponding zoomed area in the original image.

5.1.5 Low Light conditions and Rain, Fog and Snow (CNF 13, 14, 15)

It is unavoidable to drive in conditions where the ambient light levels are low, especially during night conditions, areas with big shades, tunnels, harsh weather, etc. Whilst artificial light can illuminate specific areas in a driving scene, it cannot cover the whole camera's FoV. There is a significant amount of work in deep neural networks to enhance, change, and adapt the luminosity of camera frames, so we opted for a cycleGAN, and suitably trained it to transform 'well illuminated' images into low light ones [15] [9]. The visual content of the scene itself is affected by the luminosity, therefore the cycleGAN transformation is applied prior to the weather models. However, luminosity of the scene plays a role in the appearance of the weather, therefore as the luminosity of the scene is lower, the luminosity parameter of the weather models needs to be adjusted accordingly, see Figure 20.

The effect of the weather is based on the luminosity and appearance of the captured scene. Under low light conditions, the scene is significantly darker and with decreased contrast, hence the weather's appearance and particularly the particles' streaks are less noticeable. Again, fog seems to interact strongly with low light, and even the white car is barely identifiable when the compound noise is applied, a dark target in the same position would be probably almost disappear in the frame.

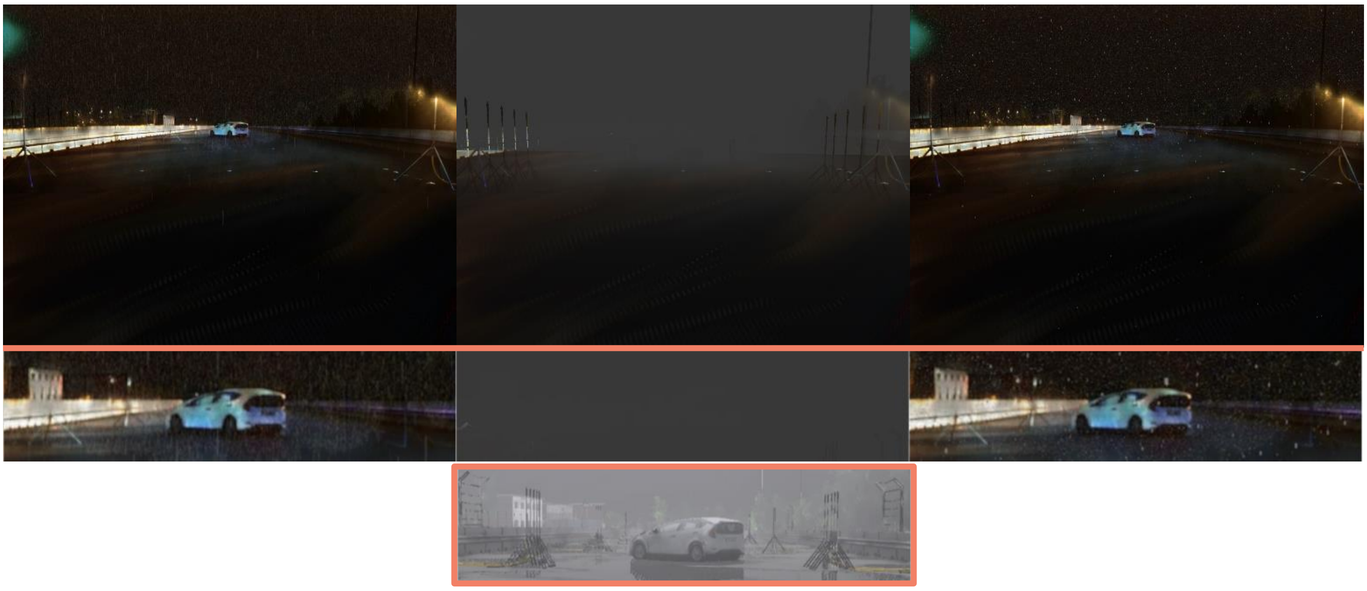

Figure 20: Weather model compounded with low light transformations. Left: Rain. Middle: Fog. Right: Snow, Middle row: zoomed in area of the frame. Bottom row, corresponding zoomed area in the original image.

5.1.6 Wind and Rain, Fog and Snow (CNF 16, 17, 18)

When wind is present during adverse weather such as rain, for and snow, the wind results in a force on the weather particles, altering the droplet path. Assuming that the wind is consistent, a new terminal velocity (balancing the force against drag where the particles are considered as spheres) can be calculated for the raindrop to determine the total speed of the droplet. As wind directly interacts with the weather, a sequential application of noise cannot be used. Instead, the wind impacts the movement of the droplet, hence the part of the rain, fog and snow weather models governing the streak appearance of each droplet is modified to include the motion of the droplets due to wind, see Figure 21. If the wind is blowing along the vehicle direction, it will have only an effect of slightly elongating or shortening the streaks. If the wind is blowing sideways, the the streaks will appear oblique, as shown in the figure below. A crosswind speed of 3 ms^{-1} (10.8 kmh^{-1}) was applied for compounding in Figure 21.

The effect of side wind results in sideways motion of particles for rain and snow. The increase in the forces acting on snow results in the streaking shown in the snow-wind compounded image. At the same wind speed, the streak for snow is shorter with less sideway motion due to the low density which reduces the terminal speed. Fog droplets are dense and small in nature. Combined with the static property of the particles, any movement of particles arising from the wind would be minor and not captured in an image.

Figure 21: Weather model compounded with a wind model. Left: Rain. Middle: Fog. Right: Snow. Middle row: zoomed in area of the frame. Bottom row, corresponding zoomed area in the original image.

5.2 LiDAR and 4D RADAR

Table 6 presets 3 additional noise factors that can be applied to LiDAR or 4D RADAR point clouds in combination with the weather models presented in D3.4. This subsection presents these additional models and the compounded effects on the point clouds when modelling both the weather and the noise factors. LiDAR and 4D RADAR are both active sensors and output data in a similar format, so the methodology of compounding noise models is applied in a similar fashion, but the effects of the different considered noise factors can be significantly different given the specific electro-magnetic wavelengths used. For weather models, the parameters are set to high precipitation levels for better visibility. Accordingly, the fog visibility distance is set to 30 m, the rain intensity to 20 mm/h, and the snow rate to 2.5 mm/h.

5.2.1 LiDAR: Laser Alignment Error and Rain, Fog and Snow (CNF 19, 20, 21)

Laser alignment error in automotive Lidar arises from discrepancies between the sensor's calibration and factory values, often caused by wear, environmental factors, or manufacturing tolerances. As a part of ROADVIEW, we have used a dedicated setup to measure in a systematic way this error and then fitted the results to create a data driven model. The measured error is well fitted as a normal distribution, the ROADVIEW model samples this distribution, and add the sampled noise value to each point of the ideal point clouds to simulate its impact.

To compound the additional alignment error model with weather models, the alignment error is applied first, followed by the weather models. This sequence reflects the process where the emitted light is initially affected by alignment errors before being influenced by environmental conditions. Overall, the combination of the alignment error with the weather models causes a significant degradation in the point cloud, where not only we can observe an increased number of particles detected in the very short range, increased sparsity and decreased long range detection, but also overall the spatial distribution of points in the point cloud is less accurate than in the 'ideal' data.

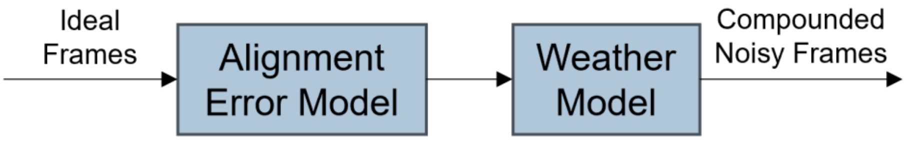

Figure 22: Compounding Order.

The measured error, represented as normal distribution, equals to $\mathcal{N}(0°,\ 0.001°)$ for azimuth angles and $\mathcal{N}(0°,\ 0.127°)$ for elevation angles.

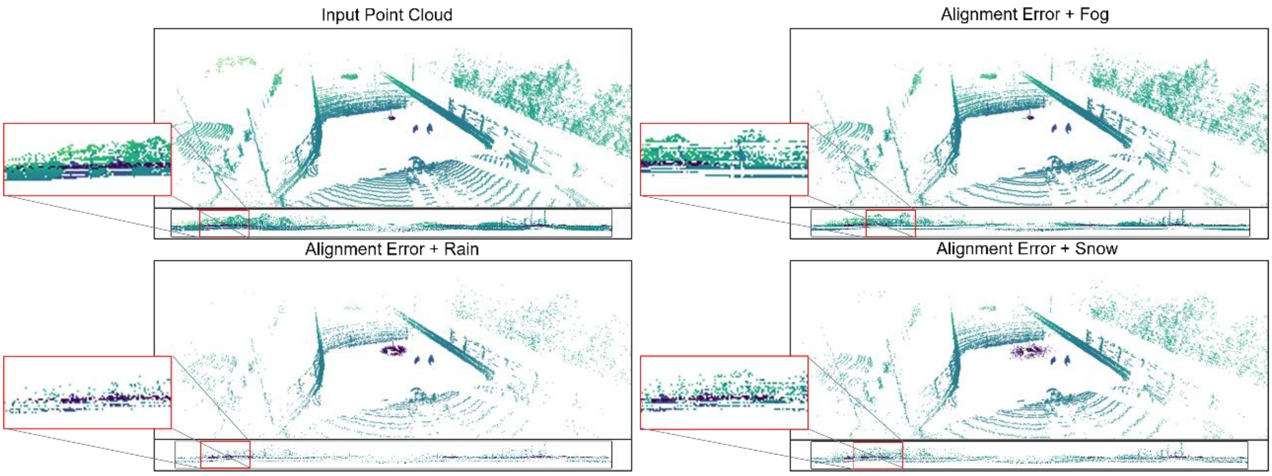

Figure 23: Results of the compounded alignment error and weather model. The colour of the points represents their respective depth.

5.2.1.1 RADAR: Alignment Error and Rain, Fog and Snow

A similar process to the one described above can be applied to 4D RADAR point clouds, however the experiments might be affected by multi-path reflections and other errors caused by using the RADAR in an enclosed environment, so we believe that more work needs to be done with RADAR sensors suppliers to have an accurate modelling of this kind of error.

5.2.2 LiDAR: Laser Power Variance and Rain, Fog and Snow (CNF 22, 23, 24)

Laser power variance refers to the fluctuation or reduction in a Lidar system's laser output over time. This variance can be caused by aging of laser diodes and components, thermal effects impacting efficiency, variation in power supply, or environmental factors like dust, humidity, and vibrations. These changes can reduce the system's range and accuracy, making it essential to consider laser power variance in Lidar noise modelling to ensure reliable performance throughout its lifespan.

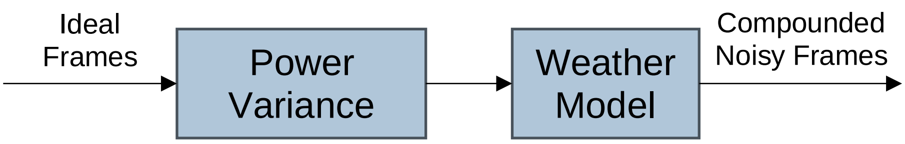

Figure 24: Compounding Order.

To compound the power variance model with weather models, the power variance model is applied first, followed by the weather models. This sequence mirrors the real-world process where the emitted light is initially affected by power-related noise before being further influenced by environmental conditions. Overall, the combination of the power error with the weather models causes a significant degradation in the point cloud, where not only we can observe an increased number of particles detected in the very short range, increased sparsity and decreased long range detection, but also overall the detection of further or small objects seems degraded, particularly for rain and snow. The measured power error, represented as normal distribtuion, equals to $\mathcal{N}(0,\ 5)$ which is applied to LiDAR intensity values.

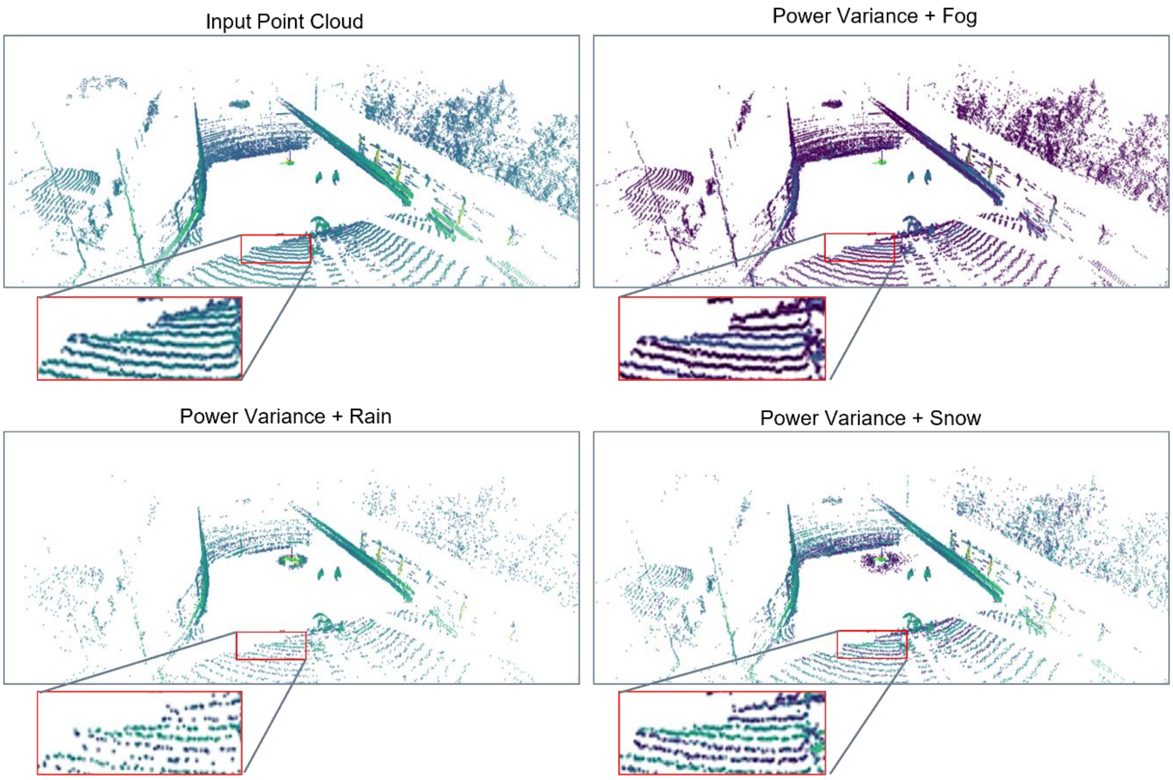

Figure 25: Results of the compounded power variance and weather model. The colour of the points represents their respective laser intensities.

5.2.2.1 RADAR: Power Error and Rain, Fog and Snow

A similar process to the one described above can be applied to 4D RADAR point clouds, however the experiments might be affected by multi-path reflections and other errors caused by using the RADAR in an enclosed environment, so we believe that more work needs to be done with RADAR sensors suppliers to have an accurate modelling of this kind of error.

5.2.3 LiDAR and 4D RADAR: Lens obstruction and Rain, Fog and Snow (CNF 25, 26, 27)

Lens obstruction in automotive LiDAR sensors occurs when contaminants such as dust, mud or other debris accumulate on the sensor's surface, partially blocking its field of view [16]. This phenomenon is a result of the sensor's exposure to various environmental conditions during vehicle operation and might have different implications depending on the positioning of the sensor. As a proof of concept, lens obstruction is simulated as random patches on the depth-image view of the point clouds, for easy of visualisation we used square patches, but we can apply random shape pattern in a similar way to what has been shown for camera, see 5.1.1. These simulated obstructions can vary in size and intensity to represent different types of contaminants. For instance, smaller patches might represent dust particles, while larger ones could simulate mud splatter or water droplets. The placement of these patches is randomised to mimic real-world scenarios where contamination can occur unpredictably across the sensor's surface.

To compound the obstruction model with weather models, the obstruction model is applied after the weather models. This is because the weather models account for the dropped rays, so they should be applied first and then the rays should be blocked as they reach the sensor.

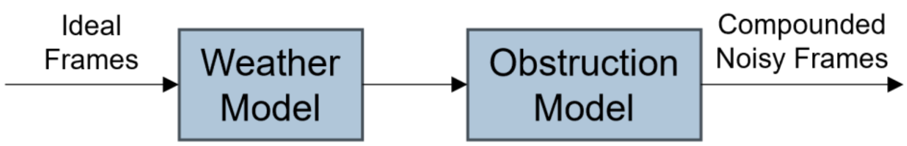

Figure 26: Compounding Order.

Overall, these two types of noise (weather and obstruction do not interact significantly – it is possible to observe the effect of weather on the points and then some regions in the point cloud with ‘holes’ due to the blocked LiDAR channels. Similarly to camera obstruction, the obstructions on LiDAR and 4D RADAR can have more or less severe consequences depending on their size and positioning. The probability that a random patch obstructs a laser beam (emitter and receiver) on LiDAR's sensor surface is set to 6×10^{-5}.

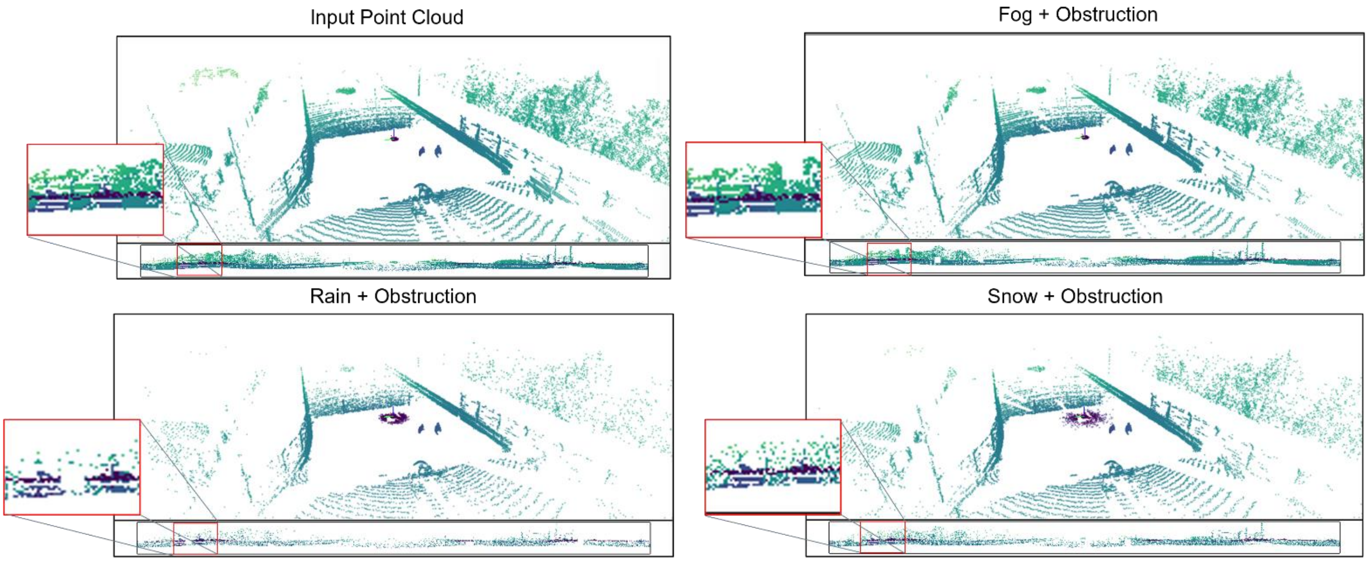

Figure 27: Results of the compounded obstruction and weather model. The colour of the points represents their respective depth.

The similar approach of the one discussed above can be used for 4D RADAR point clouds to simulate obstruction on the sensor, as shown in figure. The probability that a random patch obstructs a region on 4D RADAR's sensor surface is set to 2×10^{-3}.

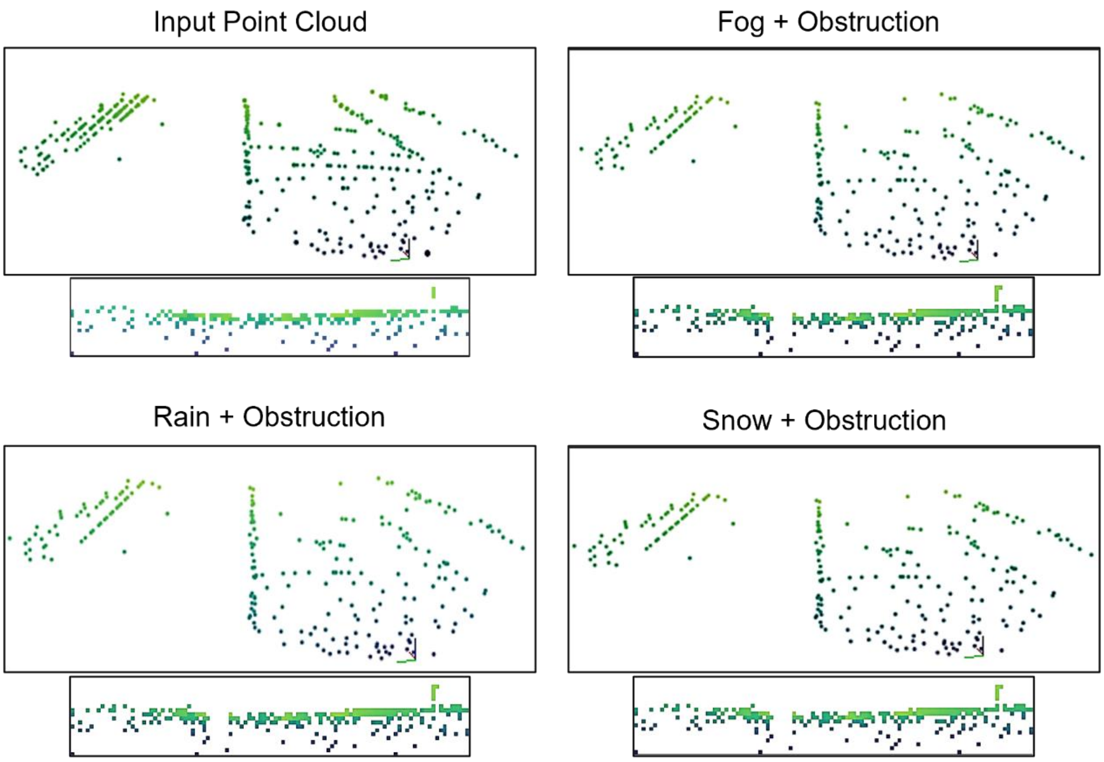

Figure 28: Results of the compounded obstruction and weather model for 4D RADAR. The colour of the points represents their respective depth.

5.2.4 LiDAR: Laser Raydrop (CNF 28, 29, 30)

Real Lidar scans often exhibit patterns of missing points, commonly referred to as the raydrop effect. This occurs when emitted laser rays either fail to return or return with insufficient power for the receiver to detect them. The phenomenon typically arises when rays exceed the maximum detection range without interference or encounter highly reflective or refractive surfaces. To simulate this effect, we employ a machine learning-based model that predicts which points are likely to be missed on ideal simulated scans, following an approach similar to that proposed by Guillard et al. [10]. This model is of particular importance when using simulated 'ideal' point clouds, as applying raydrop noise model can make the point clouds look less 'perfect' and more 'real'.

To compound the raydrop model with weather models, the raydrop effect is applied first, followed by the weather models. This sequencing ensures that the weather model, a post-processing approach, accounts for missed points and determines their potential interaction with weather conditions.

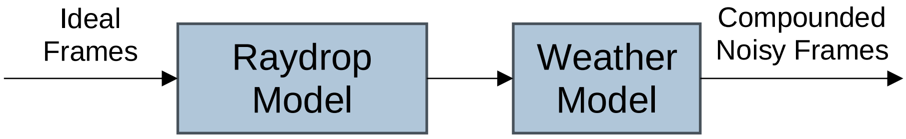

Figure 29: Compounding Order.

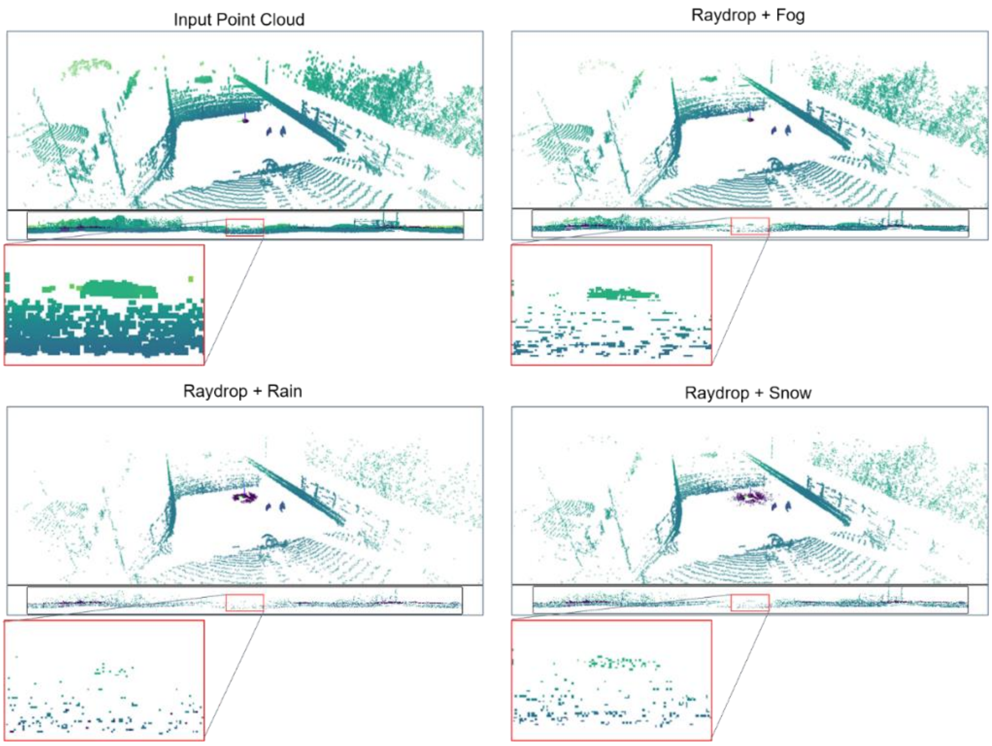

Figure 30: Results of the compounded raydrop and weather model. The colour of the points represents their respective depth.

6 Conclusions

In ROADVIEW Task 3.5, a framework was developed and used to compound a total of 30 different weather and noise factor pairs. The method of compounding was carefully considered depending on the specific selected noise factors, and the methodology of compounding is described in this report. A core contribution of this work was the demonstration of the different compounding methodologies and how each noise combination can further degrade the sensor data and create corner cases. The compounded models were applied to images formed from camera sensors and point clouds formed from LiDAR and 4D RADAR sensors. This work applied the framework on pointcloud predominantly from LiDAR, as LiDAR is overall more affected by the weather conditions than 4D-RADAR, as shown in the Deliverable 3.4. However, the proposed compounding methodology can be applied to 4D-RADAR, as shown for example for the occlusion noise with the application order arrangement of the noise factors being very similar to LiDAR. This has been demonstrated on the generated 4D RADAR pointcloud generated by the ROADVIEW 4D RADAR model that is integrated into the ROADVIEW CARLA by WMG, THI, and LUA.

The report and the application of the compounded noise models demonstrates that there are varying effects from the compounding of noise factors. As observed in Chapter 5, some compounded models exacerbate the degradation in the image, whilst others cover up and hide the effect of the weather. Additionally, the set intensity of the noise models will also affect the image differently, potentially causing interesting corner cases. For example, the occlusion model causes parts of the sensor data to be fully blocked (i.e. missing). For heavy occlusion, it could cover up most of the captured sensor data, but a lighter occlusion coverage can cause objects to fade in and out of the sensor data.

For camera, the effect of compounding affects each of the three weather noise factors differently. In general, rain streaks can make distortions noticeable, e.g. due to lens distortion, wind, etc. Due to the smaller size of snow particles, any blurring effects are likely to reduce or remove the visible snow. For fog, many of the noise factors investigated here had minor or no impact effect of the fog appearance. However, due to the fog attenuation, lossy compression can cause severe degradation and strongly impact the resulting image. One difficulty in the combining multiple sources of noise for camera is the lack of availability of models in the Bayer space. Not all models can be applied to the Bayer image without introducing prominent artefacts. Whilst this work converts between Bayer and coloured image based on the need of the model, future work on noise modelling and compounding should be focused on Bayer rather than coloured images.

For LiDAR, fog simulation generally does not significantly change the point clouds, except in cases of power variance, where its effects become more noticeable. However, fog heavily attenuates the power, and this attenuation makes power variance effects more prominent. Additionally, rain simulation typically causes more points to be dropped compared to snow. This is because rain combines the effects of water droplets and fog, resulting in greater power attenuation and, consequently, more missing points.

The result of the compounding demonstrates that it is simply not enough to apply one noise model at a time but to be able to correctly simulate multiple noise to stress test the system. The models and compounding method can be used in the testing pipeline of WP7 to increase the conditions for stress testing the system and reduce the simulation to reality gap. The compounded models can support the XiL testing in WP7 by providing more complex noise to be simulated in virtual testing. Additionally, the addition of compounded noise can be used to augment images with a variety of noise sources to improve the robustness of algorithms and support the tasks in WP4 and WP5.

7 References

[1] T. Herranen and A. Kloek, “D3.1 Implementation of digital twins,” ROADVIEW, 2023.

[2] P. Duthon, H. Ouattara, S. Liandrat and Y. Poledna, “D3.3 Library of validated statistical noise models,” ROADVIEW, 2024.

[3] P. H. Chan, J. Robinson, D. Gummadi, Y. Poledna and V. Donzella, “D3.4 Library of validated physics-based parameterised noise models,” ROADVIEW, 2024.

[4] P. H. Chan, G. Dhadyalla and V. Donzella, “A Framework to Analyze Noise Factors of Automotive Perception Sensors,” IEEE Sensors Letters, vol. 4, no. 6, pp. 1-4, 2020.

[5] B. Li, P. H. Chan, G. Baris, M. D. Higgins and V. Donzella, “Analysis of Automotive Camera Sensor Noise Factors and Impact on Object Detection,” IEEE Sensors Jouirnal, pp. 22210-22219, 2022.

[6] P. H. Chan, S. Shahbeigi, X. Ye and V. Donzella, “A noise analysis of 4D RADAR: robust sensing for automotive?,” TechRxiv, p. 10, 2023.

[7] G. Baris, B. Li, P. H. Chan, C. A. Acizzano and V. Donzella, “Analysis of Faster R-CNN network prediction in the presence of lens occlusion and video compression,” Authorea Preprints, pp. 1-13, 2023.

[8] A. Senyaev, A. Smorkalov, Grigory and O.-P. Heinisuo, “opencv-python 4.10.0.84,” 17 June 2024. [Online]. Available: https://pypi.org/project/opencv-python/4.10.0.84/.

[9] Y. Wang, H. Zhao, K. Debattista and V. Donzella, “The Effect of Camera Data Degradation Factors on Panoptic Segmentation for Automated Driving,” in 2023 IEEE 26th International Conference on Intelligent Transportation Systems (ITSC), Bilbao, Spain, 2023.

[10] B. Guillard, S. Vemprala, J. K. Gupta, O. Miksik, V. Vineet, P. Fua and A. Kapoor, “Learning to Simulate Realistic LiDARs,” in 2022 IEEE/RSJ International Conference on Intelligent Robots and Systems (IROS), Kyoto, Japan, 2022.

[11] Velodyne, “Alpha Prime User Manual,” Velodyne, 2023.

[12] J. C. Lagarias, J. A. Reeds, M. H. Wright and P. E. Wright, “Convergence properties of the Nelder - Mead simplex method in low dimensions,” SIAM Journal on Optimization, vol. 9, no. 1, pp. 112-147, 1998.

[13] M. Uřičář, J. Ulićný, G. Sistu, H. Rashed and D. Hurych, “Desoiling Dataset: Restoring Soiled Areas on Automotive Fisheye Cameras,” in 2019 IEEE/CVF International Conference on Computer Vision Workshop (ICCVW), Seoul, South Korea, 2019.

[14] P. H. Chan, A. Huggett, G. Souvalioti, P. Jennings and V. Donzella, “Influence of AVC and HEVC Compression on Detection of Vehicles Through Faster R-CNN,” IEEE Transactions on Intelligent Transportation Systems, vol. 25, no. 1, pp. 203-213, 2024.

[15] J.-Y. Zhu, T. Park, P. Isola and A. A. Efros, “Unpaired Image-to-Image Translation Using Cycle-Consistent Adversarial Networks,” in 2017 IEEE International Conference on Computer Vision (ICCV), Venice, Italy, 2017.

[16] S. Son, W. Lee, H. Jung, J. Lee, C. Kim, H. Lee, S. Cho, J. Jang, M. Lee and H.-C. Ryu, “Experimental Analysis of Various Blockage Performance for LiDAR Sensor Cleaning Evaluation,” Sensors (MDPI), 2023.

Appendix A
LiDAR noise factors breakdown

A LiDAR noise framework breakdown by Chan et al. [4].

Factor Type	ID/ Noise Factor	Intensity	Time of Flight	Angle of Emission	Position
Piece to Piece	01. Laser Diode	✓	✓		
	02. Mounting			✓	
Change over Time	03. Emitter	✓	✓		
	04. Mechanics			✓	
	05. Receiver	✓	✓		
	06. Circuits	✓	✓		
Usage	07. Multiple Returns	✓			✓
	08. Motion				✓
	09. Clock Speed		✓		
	10. Lens Damage	✓			✓
Environment	11. Weather	✓	✓		
	12. Obstruction	✓			✓
	13. Ambient Conditions	✓	✓		
System Interactions	14. Malicious Attacks	✓			✓
	15. Mutual Interference	✓			✓
	16. EMI	✓	✓		✓

Appendix B
Camera noise factors breakdown

A camera noise breakdown by Li et al. [5].

Factor Type	ID/ Noise Factor	Frame Rate	Intensity	Position	Dropped Frames
Piece to Piece	01. Alignment		✓	✓	
	02. Fabrication Variability	✓	✓		
	03. Lens shape, purity		✓	✓	
	04. Dark Current variability		✓		
	05. Image Signal Processing	✓	✓	✓	
Change over Time	06. Ageing of electronics	✓	✓		
	07. Degradation of Lens		✓	✓	
	08. Vibration of Mounting		✓	✓	
	09. Pollutant Ingress		✓	✓	✓
	10. Pixel Degradation		✓		
	11. Board Ageing	✓	✓		✓
Usage	12. Misplacement of the sensor		✓	✓	
	13. Vehicle impact		✓	✓	
	14. Chemicals/ Contaminants		✓	✓	
	15. Obstructions		✓	✓	
	16. Lens Scratch		✓	✓	
	17. Vehicle dynamic settings		✓	✓	
Environment	18. Sensor saturation or depletion		✓		
	19. Extreme Temperature	✓	✓		✓
	20. Adverse Weather		✓		
	21. Optic Obstructions		✓	✓	
	22. Low Illumination		✓		
	23. Sun		✓		
System Interactions	24. Malicious Attacks	✓	✓	✓	✓
	25. Windshield			✓	
	26. Power Supply	✓	✓		✓
	27. EMI	✓	✓		✓
	28. Saturation of Buffer		✓	✓	✓
	29. LED flicker		✓		
	30. Localised Light source		✓		